Numerical Investigation of Rotorcraft Fuselage Drag Reduction using Active Flow Control

Brian G. Allan and Norman W. Schaeffler
NASA Langley Research Center, Hampton, VA

The effectiveness of unsteady zero-net-mass-flux jets for fuselage drag reduction was evaluated numerically on a generic rotorcraft fuselage in forward flight with a rotor. Previous efforts have shown significant fuselage drag reduction using flow control for an isolated fuselage by experiment and numerical simulation. This work will evaluate a flow control strategy, that was originally developed on an isolated fuselage, in a more relevant environment that includes the effects of a rotor. Evaluation of different slot heights and jet velocity ratios were performed. Direct comparisons between an isolated fuselage and rotor/fuselage simulations were made showing similar flow control performance at a -3° fuselage angle-of-attack condition. However, this was not the case for a -5° angle-of-attack condition where the performance between the isolated fuselage and rotor/fuselage were different. The fuselage flow control resulted in a 17% drag reduction for a peak C_μ of 0.0069 in a forward flight simulation where $\mu = 0.35$ and $CT/\sigma = 0.08$. The CFD flow control results also predicted a favorable 22% reduction of the fuselage download at this same condition, which can have beneficial compounding effects on the overall performance of the vehicle. This numerical investigation was performed in order to provide guidance for a future 1/3 scale wind tunnel experiment to be performed at the NASA 14-by 22-Foot Subsonic Tunnel.

Nomenclature

A_{CS}	=	fuselage body cross-sectional area (maximum), inches
A_j	=	jet slot area, inches
a_∞	=	freestream speed of sound, ft/s
C_D	=	fuselage drag coefficient, $D/(q_\infty A_{CS})$
C_L	=	fuselage lift coefficient, $L/(q_\infty A_{CS})$
C_p	=	pressure coefficient, $(p-p_s)/q_\infty$
C_T	=	rotor thrust coefficient, $T/\rho_\infty \pi R^2 (\Omega R)^2$
C_T/σ	=	blade loading coefficient
C_μ	=	jet momentum coefficient, $\sum(\dot{m}_j U_j)/(q_\infty A_{CS})$
D	=	drag force, lbs
f	=	excitation frequency, Hz
F^+	=	reduced frequency, fW/U_∞
h	=	jet slot height, inches
H	=	fuselage main body height (maximum)
L	=	lift force, lbs
M	=	Mach number, U_∞/a_∞
p	=	pressure. psi
p_s	=	static pressure,psi
q_∞	=	freestream dynamic pressure, $1/2\rho_\infty U_\infty^2$, psi
R	=	rotor radius, inches
R_F	=	reference rotor radius, inches
Re	=	Reynolds number, $U_\infty(2R_F)/\nu$
U_∞	=	freestream velocity, ft/s
U_{tip}	=	rotor tip hover velocity, ft/s
U_j	=	jet exit velocity, ft/s
VR	=	jet velocity ratio, U_j/U_∞
w	=	width of surface blowing boundary condition, inches
W	=	fuselage body width (maximum), inches
x/R_F	=	normalized streamwise coordinate
y/R_F	=	normalized cross-stream coordinate
z/R_F	=	normalized vertical coordinate
$ZNMF$	=	Zero-Net-Mass-Flux
α_j	=	jet inclination angle, degrees
ϕ	=	jet phase angle, degrees
ψ	=	rotor azimuth angle, degrees
α	=	angle of attack, degrees
α_j	=	jet inclination angle, degrees
α_s	=	rotor shaft angle, degrees
μ	=	rotor advance ratio, $U_\infty \cos\alpha/(\Omega R)$
ν	=	kinematic viscosity, ft^2/s
ρ	=	density, $slugs/ft^3$
ρ_j	=	jet density, $slugs/ft^3$
σ	=	thrust weighted rotor solidity

Subscripts

j	=	jet
∞	=	freestream

Presented at the American Helicopter Society 67th Annual Forum, Virginia Beach, VA, May 3-5, 2011.

THE design of a rotorcraft fuselage shape places greater emphasis on function than on aerodynamic efficiency, typically resulting in designs that experience significant drag at cruise. The cruise drag of a rotary-wing aircraft is

an order of magnitude higher than the cruise drag of a fixed-wing aircraft of the same gross weight (Ref. 1). At high advance ratios, half the power to the main rotor is used to overcome the fuselage drag (Ref. 2). The drag force acting on a rotorcraft fuselage that features an aft-facing ramp is typically dominated by massive flow separation on the rear of the fuselage. This results in a large pressure drag contribution to the total drag force. The shear layers emanating from the separated region tend to roll-up in an unsteady fashion. This, in turn, results in unsteady aerodynamic loadings on the tail boom, stabilizers and tail rotor. By applying active flow control (AFC) to the ramp region of the fuselage, the size of the fuselage wake can be reduced, lowering the drag and reducing the undesirable unsteady loading on the downstream structures of the rotorcraft. Previous research in this area has demonstrated the importance of considering the impact of any drag reduction on the download that the fuselage develops. The works Martin, et al. (Ref. 3) and Ben-Hamou et al. (Ref. 4) demonstrated a fuselage drag reduction through the application of active flow control, by 20% and 11% respectively. Martin, et al. went on to show the profound effect that AFC can have on download reduction. Since in a rotorcraft system the rotor is responsible for both thrust and lift, a benefit from a reduction in drag may be offset by an increase in download, effectually limiting any benefit from applying the flow control.

In order to investigate different fuselage drag reduction approaches, an integrated experimental and computational research effort was undertaken under the NASA Subsonic Rotary Wing (SRW) Project utilizing a generic fuselage as its basis. A new generic fuselage was developed for this effort called the ROBIN-mod7. It is a modified version of the ROBIN (ROtor Body INteraction) fuselage that was developed at NASA Langley in the 1970's to be representative of a generic helicopter and also to be easily reproduced for calculations (Ref. 5). The original ROBIN fuselage is well-documented in wind tunnel investigations (Refs. 6, 7) and is a popular generic fuselage within the rotorcraft CFD community (Refs. 8, 9). The fuselage calculation procedure and the modified coefficients for the ROBIN-mod7 are discussed fully by Schaeffler et al. (Ref. 10). It is intended that the ROBIN-mod7 fuselage can be established as a standard test fuselage for evaluating different AFC strategies both experimentally and computationally.

The integrated experimental and computational approach of this work allowed the baseline aerodynamic characteristics to be documented and validated simultaneously (Ref. 10). Out of this effort and a related collaboration between NASA and ONERA, a flow control strategy was identified for the isolated fuselage which produced a 26% drag reduction using unsteady zero-net-mass-flux (ZNMF) jets (Ref. 10). The next step in this work is to see how the developed strategy is affected by increases in Reynolds number and by the effect of the rotor downwash. To accomplish this, a wind tunnel test is planned in the NASA 14-by 22-Foot Subsonic Tunnel. The research reported in this paper involves numerical simulations using a Reynolds-averaged Navier-Stokes (RANS) flow solver in support of this future wind tunnel entry. The investigation takes the lessons learned from the flow control strategies developed on the isolated fuselage and applies them to the more relevant environment of a fuselage and rotor operating at a high advance ratio. This allows for the study of the affect of the rotor and its downwash on the fuselage drag and download and on the effectiveness of the active flow control for elevating some of the drag and download forces. Additionally, results from this investigation will provide guidance on the flow control approach and identify slot configurations and flow control actuator parameters such as slot size, frequency, and peak jet velocity as well as to identify critical measurements needed for CFD validation.

Numerical Modeling Approach

Flow Solver

The flow field for the fuselage was computed using the flow solver code, OVERFLOW (Refs. 11, 12) developed at NASA. This code solves the compressible RANS equations using the diagonal scheme of Pulliam and Chaussee (Ref. 13). The RANS equations are solved on structured grids using the overset grid framework of Steger, Dougherty, and Benek (Ref. 14). The flow is computed on node-centered grids composed of curvilinear body-fitted grids overset onto automatically generated Cartesian block background grids. Convergence and accuracy of the flow solution was improved using a Low-Mach number Preconditioning (LMP) option for steady simulations. The numerical simulations were performed using the parallel version of the OVERFLOW code developed by Buning (Ref. 15). This code uses the Message-Passing Interface (MPI) and can run on a tightly-coupled parallel machine or a network of workstations. The code distributes zones to individual processors and can split larger individual zones across multiple processors using a domain decomposition approach.

The RANS equations are solved implicitly using the Beam-Warming block tridiagonal scheme with a 3^{nd} order Roe upwind scheme for the inviscid flux terms. The Spalart Allmaras (SA) turbulence model was used for the numerical simulations (Refs. 16, 17). A Rotational/Curvature Correction (RCC) model, as implemented in OVERFLOW, was used to correct the SA model for surface curvature effects (Ref. 18). The RCC model was shown in the previous effort to improve the symmetry of the baseline flow simulations and had a significant performance impact on simulations with small AFC slots.

The blowing jets in OVERFLOW were simulated using a surface boundary condition, simplifying placement of the jets on the fuselage. Since the blowing slots intersect the fuselage surface at an angle, α_j, the width of the jet surface

boundary condition is:

$$w = h/\sin(\alpha_j) \tag{1}$$

where w is the width of the blowing boundary condition on the fuselage surface and h is the idealized flow control slot height. The jet blowing angle is based on the local surface tangent, normal to the slot span. An $\alpha_j = 90^\circ$ is therefore normal to the local surface and $\alpha_j = 0^\circ$ is tangent to the local surface and normal to the slot local spanwise tangent. The jet properties were defined by setting a mass flow ratio per unit area of, $\rho_j U_j/\rho_\infty U_\infty$, and the total temperature ratio, $T_{tj}/T_{t\infty}$. Unsteady ZNMF jets were simulated by modifying the surface boundary condition using a sinusoidal fluctuation term defined as:

$$U_j(t) = VR\, U_\infty \sin(2\pi f t + \phi) \tag{2}$$

where f is the frequency, ϕ the phase, and VR is the peak jet velocity ratio.

Grids

The grids, shown in Figs. 1 and 2, included five fuselage grids with eight refined overset grids to resolve the flow control blowing on the surface and twelve grids for the four rotor blades. The rotor and body wakes were captured using grids that have a uniform grid spacing equal to 10% of the rotor tip chord in all three directions. These wake grids extended $0.8R$ downstream of the rotor tip path plane and $0.8R$ below the rotor hub center, capturing the rotor and fuselage wake. Automatic background grids were generating by OVERFLOW and coarsened by doubling the cell size for each successive level of grids that extended the far field computational domain. This procedure was used until the far field boundary was extended approximately $52R$ away from the hub center. The numerical simulations had a total of 160 million grid points, including 40 million grid points used for the body and rotor volume grids.

Fuselage and Rotor Blade Geometries

The ROBIN-mod7 geometry is shown in Figure 3 along with model dimensions for the joint U.S. Army and NASA forward flight test to be conducted in the 14-by 22-Foot Subsonic Tunnel at NASA Langley. The fuselage geometry for the forward flight test is the same as the isolated fuselage experiment of Schaeffler et al. (Ref. 10) with the added inclusion of an upper pylon that partially encloses the rotor shaft. The model for the isolated fuselage test had a fuselage length of 28.24" as compared to a length of 123.931" for the planned forward flight test fuselage. The Reynolds number, based on the fuselage length of the forward flight test, will range from 11-16 million, an order of magnitude larger than the 1.6 million of the previous isolated fuselage test.

The rotor blades were acquired specifically for a PSP validation test and were used in a recent hover test of Wong et al. (Ref. 19) at the 14-by 22-Foot Subsonic Tunnel Rotor Test Cell. The blade uses Government RC-series airfoils with the planform shown in Figure 4. The rotor has a radius of 66.5" and a linear twist of -14°. The blade has a chord length of 5.45" with a 30° tip sweep and a 3.27" tip chord length. Figure 4 show a notch in the planform from blade station 7.87 to 16.75. This notched out area contains a connector fairing to accommodate wiring from the blade pressure measurements on all four blades and is shown in Figure 4. The flap and lead-lag hinge are collocated 3.00" from the hub center.

The ROBIN fuselage was originally developed using the radius, of the rotor paired with the fuselage as a parameter for the non-dimensional description of the fuselage geometry. The length of the fuselage is defined as twice the rotor radius and the cartesian coordinates used to define the fuselage surface are all non-dimensionalized by this paired-rotor radius. Over the years, the ROBIN fuselage has been paired in wind tunnel tests with rotors that are either under or oversized based upon this non-dimensionalization. The current research effort is not an exception to this. The PSP rotor is oversized for the current fuselage by 7.3%. The scaling radius for the fuselage, R_F, is 61.9655 inches versus the PSP rotor radius, R, of 66.50 inches.

Flight Conditions

The goal of this investigation is to reduce the fuselage drag at high speed cruise where the fuselage drag is a significant portion of the entire vehicle drag. An advance ratio of $\mu = 0.35$ was selected as a typical cruise condition for maximum range with $C_T/\sigma = 0.08$. The hover tip Mach number for this investigation is 0.598 and the freestream Mach number is 0.2093. The shaft tilt angle of the rotor with respect to the fuselage is fixed at an angle of -3° for the wind tunnel model and hence was also fixed for all of the CFD simulations. An α =-3° was used as the primary simulation condition with some CFD simulations performed at α = -5°. The α = -3° and -5° corresponds to a rotor shaft angle, α_s, of -6° and -8° respectively and are typical of rotorcraft cruise for maximum range. For comparison purposes, α = -3° and -5° for the isolated fuselage cases were also simulated with and without flow control in addition to an $\alpha = 0^\circ$ baseline isolated fuselage case.

Results

Isolated Fuselage Baseline

The fuselage without a rotor was simulated to better understand the effects of the rotor on the fuselage with and without flow control. The isolated fuselage simulations have a freestream Mach number of 0.2093 with a Reynolds number based on the fuselage length of 14.9 million, matching

the rotor/fuselage flow conditions. The isolated fuselage was evaluated at $\alpha = 0^\circ$, -3°, and -5° to compare with the rotor/fuselage simulations. The $\alpha = 0^\circ$ case was simulated by solving the steady-state RANS equations and had good convergence in the RANS equation residuals. The steady-state solution for the α = -3° case did not converge as well. In this case, the drag had a sudden jump after many iterations to a different flow state and a much higher drag coefficient. This jump in the drag and lift convergence histories can be seen in Figs. 5 and 6 respectively. As seen in the drag history plot in Fig. 5, the drag coefficient converges to approximately 0.1 after 30,000 iterations. At this point the drag seems converged, however the lift history has not. Additional flow solver iterations result in a drag rise that eventually converges after 75,000 iterations for both the drag and lift coefficients.

This sudden drag rise between the flow states in the steady-state solution and the lack of convergence of the residual prompted a time-accurate flow analysis of the isolated fuselage at α = -3°. The unsteady flow simulation for the α = -3° case was initiated from a freestream condition with the time history of the drag and lift convergence presented in Figs. 7 and 8. Initially the unsteady flow simulation was run using a non-dimensional time step of DT=0.58, where DT is non-dimensionalized by the hover tip velocity and the unit grid length of one inch. Using this time step, C_D converges to 0.1 as seen in the drag history plots. Looking at the unsteady simulation results, it was noticed that there was an unsteadiness at the juncture of the upper pylon and fuselage causing an unsteadiness in the juncture vortex that interacts with the flow in the ramp region. Decreasing DT by half to a value of 0.29, the unsteadiness of the juncture vortex was arrested while the flow in the ramp region became unsteady. This unsteady flow on the ramp increased the mean drag by 20% where the forces on the body become periodic after $tU_\infty/2R_F = 30$ as shown in Figs. 7 and 8.

The isolated fuselage was then repositioned to α = -5° where the flow was initiated using the α = -3° flow solution. The results of the drag and lift histories are shown in Figs. 7 and 8 starting at $tU_\infty/2R_F = 40$. The unsteady drag history indicates that the flow is fairly unstable and converges to a periodic flow state at $tU_\infty/2R_F = 67$. The flow at this point shows the juncture vortex on the upper pylon to become unsteady when viewing a time lapse animation of the surface restricted streamlines on the fuselage. Cutting the time step in half to DT=0.145 did not affect the unsteadiness of the juncture vortex from the upper pylon or change the mean drag values. Based on these CFD results there seems to be a link between the unsteadiness of the juncture vortex and the unsteadiness on the ramp region that should be explored further.

Surface streamlines and C_p values for the baseline isolated fuselage are shown in Fig. 9 for the $\alpha = 0^\circ$, -3°, and -5° cases. One of the main differences between the three fuselage angles is the interaction of the upper pylon juncture vortex on the separated flow in the ramp region. In the previous research of Schaeffler et al. (Ref. 10), the fuselage was intentionally keep as clean as possible for the CFD validation effort and did not include the upper pylon. The juncture vortex for the $\alpha = 0^\circ$ case has little interaction with the ramp flow separation as seen in Fig. 9(d, g, j). The α = -3° case in Fig. 9 does show the juncture vortex interacting with the ramp separation resulting in four different foci in the surface streamline pattern with a large suction pressure on the ramp edges. Overall, the ramp base pressure has decreased at α = -3°, as compared to the $\alpha = 0^\circ$ case, contributing to the higher drag coefficient. Decreasing the fuselage angle-of-attack to α = -5°, resulted in the juncture vortex moving to a position higher on the ramp and increasing the base pressure

Fuselage centerline C_p plots for the isolate fuselage, for three different angles-of-attack, are given in Figs. 10 and 11 for the lower and upper surface respectively. The centerline C_p profile for the lower surface has a favorable pressure gradient on the nose with an adverse pressure gradient starting at the geometric transition point from the nose to the straight body section. The pressure decreases as it approaches the ramp section with a suction peak just downstream from $x/R_F = 1.0$. The flow separates at $x/R_F = 1.07$ for $\alpha = 0^\circ$ where the pressure flattens. The centerline pressures begin to increase at $x/R_F = 1.15$, where the ramp transitions into the tail section. This increased pressure is most prominent for the -3° case and can also be seen in the ramp C_p contours in Fig. 9(h). A close-up view of the pressure suction peak at the beginning of the ramp section is shown in Fig. 12 for the three α cases. This comparison indicates that there is only a small difference in the peak suction pressures for the different angles-of-attack with the α = -3° having the largest suction pressure. The upper centerlines C_p values in Fig. 11 have a similar favorable pressure gradient on the nose section with a large adverse pressure gradient due to the upper pylon. Overall, there is little difference between the three α cases for the upper and lower surfaces with most of the differences on the nose section and where the ramp transitions into the tail.

Isolated Fuselage with Flow Control

A series of eight slots that form a nearly continuous U-shape on the ramp region of the fuselage was found to perform best out of the other slot configurations evaluated in the isolated fuselage research by NASA and ONERA (Ref. 10). This slot configuration is shown in Fig. 3 and was generated by locating the slots on the intersection of a plane at a constant $x/R_F = 1.155$. The intersecting plane was rotated 23° at $x/R_F = 1.155$ and $z/R_F = 0$ along the spanwise axis as shown in Fig. 3. This slot layout resulted in slots that are slightly downstream of the flow separation line on the fuselage ramp. Building on the prior isolated fuselage research, we will now evaluate the perfor-

mance of the flow control for the fuselage and upper pylon with and without the rotor. The primary slot height for this investigation is 0.0195". The jet is set to an angle of 25° to the local surface tangent and blows downstream and normal to the local slot spanwise vector. This jet angle was found to perform well by Schaeffler et al. (Ref. 10). The previous research did show a slight increase in performance for a 15° jet slot angle; however, this slot angle was difficult to implement experimentally. A larger slot height of 0.030" was also simulated for a select number of cases as guidance for the design of the wind tunnel model flow control slots.

The flow control simulations were initiated from their respective baseline cases using ZNMF jets with a non-dimensional frequency of $F^+ = 0.56$. This frequency corresponds to four jet blowing and suction cycles per one rotor revolution in the rotor/fuselage simulations discussed below. Based on the results from the NASA and ONERA (Ref. 10) research, each blowing slot is 180° out-of-phase from its adjacent slots. This was found to greatly minimize oscillations in the fuselage drag and provide the best drag reduction performance.

$\alpha =$ -3° **Case** The isolated fuselage drag history results, using the 0.030" slots for a VR of 1.5, resulted in a mean C_D value of 0.094 or a 22% reduction from the baseline drag. This case has a peak C_μ value of 0.0068, which is based on the maximum cross-sectional area, A_{CS}, of the fuselage body, excluding the upper pylon. The peak C_μ value is calculated using the total mass flux exiting all the slots and the peak exit velocity. Since half the jets are 180° out-of-phase from each other, only half the jets are blowing during the peak condition while the other half are at peak suction. The smaller 0.0195" slot height, for the same VR of 1.5, has a C_μ value 0.0045 and results in an overall mean drag reduction; however, this drag history switches intermediately between a C_D value of 0.10 and 0.11 as seen in Fig. 13. Increasing the VR to 2.0 for the 0.0195" slot, increases C_μ to 0.008 and removes the large unsteadiness in the drag history. The higher VR of 2.0 results in a mean drag value of 0.099, which is a 17.5% reduction from the baseline drag. It is noted that the larger slot, which has a C_μ value of 0.0068, performed better than the smaller slot at the higher C_μ value of 0.0080. Similar results were seen in the CFD simulations for the low Reynolds number investigations (Ref. 10) for steady blowing. Additional flow control simulations with the larger slot height needs to be performed in order to better understand the performance difference between the two slot sizes for the isolated fuselage. Discussions of the performance between the two slot sizes are made below in the Rotor/Fuselage with Flow Control section.

The lift results for the $\alpha =$ -3° isolated fuselage case in Fig. 14 show a reduction of the download on the fuselage. The larger 0.030" slot height with a VR of 1.5 has a mean C_L value of -0.088 as compared to the baseline mean C_L value of -0.12 and is a 28% reduction of the fuselage down load. The smaller 0.0195" slot for a VR of 1.5 had a similar mean value; however, the lift time history shows the same intermittent flow switching seen in the drag. Increasing the VR to 2.0, for the 0.0195" slot, results in a mean C_L value of -0.114 or a 7.3% reduction of fuselage baseline download force.

To better understand the effects of the flow control on the fuselage drag, a view of the surface restricted streamlines and C_p contours for the baseline and flow control cases are shown in Fig. 15. The flow control case in this figure has a slot height of 0.0195" and a VR of 2.0. This figure shows a snapshot of the flow on the ramp for a jet phase of $\phi =$ 0°, 90°, and 270°. At $\phi = 0°$, seen in Fig. 15(b), all the jets have zero velocity. Comparing the C_p contours to the baseline case in Fig. 15(a), it can be seen that the ramp base pressure has significantly increased, contributing to a fuselage drag reduction. This figure also shows a reduction of the flow separation on the ramp with an increase of the suction pressure on edges of the ramp region. This increase in the suction pressure is due to the flow being reattached on the ramp, increasing the external flow velocity on the ramp edges. This suction pressure does contribute to increasing the fuselage drag, reducing the effectiveness of the flow control jets. At $\phi = 90°$ and 270°, seen in Fig. 15(c) and (d), half the jets are at peak blowing and the other half at peak suction. These two jet phases are fairly similar to Fig. 15(b) in that the ramp base pressure is higher than the baseline case and the flow separation locations have move inward with a large suction pressure on the corners of the ramp. These two figures also show a high pressure region just downstream of the slots that are at peak blowing.

$\alpha =$ -5° **Case** Decreasing the fuselage α to -5° resulted in a loss of performance for the ZNMF flow control. Only the 0.0195" slots were simulated for this case with the drag results shown in Fig. 16. The VR of 1.86 and 2.5 both increased the mean drag coefficient with a marginal drag reduction for a VR of 3.0. While the ramp base pressure has improved for these cases, the suction pressure on the corners of the ramp have also increased. From these results it is apparent that the performance of the flow control is affected by the rotation of the fuselage to a more nose downward position. This rotation results in the suction pressure on the bottom of the ramp having a larger component in the drag direction, reducing the effectiveness of the flow control. The loss of performance for the fuselage lift is also seen in Fig. 17 where the download force on the fuselage has doubled. The nose down rotation of the fuselage also means that the increase base pressure on the ramp also has an increased downward component, contributing to the total download on the fuselage.

The surface C_p contours and streamlines for the ramp region, are shown in Fig. 18 for the $\alpha =$ -5° isolated fuselage case. Like the $\alpha =$ -3° case, the flow control is showing a

similar increased ramp base pressure with an increased suction pressure on the corners on the rear ramp. A comparison of the C_p contours between the α = -3° and -5° cases indicates similar performance for the flow control in terms of increasing the base pressure on the ramp.

To better understand the increased fuselage download using AFC for the α = -5° case, a contour plot of the difference between the surface C_p for the AFC and the baseline case, ΔC_p, are made in Figs. 19 and 20. These two figures show a bottom view of the fuselage for α = -3° and -5°. Comparing the two contour plots reveals that the α =-5° AFC case has a larger increase in the suction pressure near the ramp corners and a significant region of increased lower pressure on the tail boom, as compared to α = -3°. Therefore, the α = -5° contour plot identifies the source of the download increase as the low pressure region on the lower ramp corners and tail boom.

Isolated Fuselage Centerline Pressures The isolated fuselage centerline C_p profiles on the lower surface, with and without flow control, are shown in Figs. 21 and 22. These two figures show how the flow control increases the pressure on the centerline of the ramp as compared to the baseline case. These figures also show an increase of the suction pressure on the edge of the ramp region. Note that the flow control has also resulted in a lower pressure on the tail boom end cap with the α = -5° case having a significant decrease in pressure.

Rotor/Fuselage Baseline

The simulation of the rotor and fuselage was performed at the forward fight conditions, described in the Flight Conditions section above, for an advance ratio of $\mu = 0.35$ and rotor thrust of $CT/\sigma = 0.08$, at α = -3° and -5°. The rotor dynamics were simulated using a loose coupling between the flow solver and the comprehensive code, CAMRAD-II (Refs. 20, 21). The rotor blades are modeled as rigid blades with flapping and lead/lag motions. In the rotor/fuselage simulations, a target rotor thrust is set and the comprehensive code adjusts the collective and cyclic inputs to match the commanded thrust while minimizing flapping. The blade motions from the comprehensive code are then used in the unsteady CFD simulations. The aerodynamic forces on the rotor blades are then passed back to the comprehensive code and used to update the dynamic motion of the rotor blades and to trim the rotor, matching the target thrust while minimizing flapping. This coupling was performed every half revolution for the rotor/fuselage simulations.

The baseline fuselage drag and lift for the rotor fuselage simulations are shown in Figs. 23 and 24 for both α = -3° and -5°. The α =-3° baseline case was simulated for 9 rotor revolutions and the α =-5° case for 16 rotor revolutions allowing the fuselage drag and lift to converge. The time history showed the fuselage lift took longer than the drag to reach a converged condition. For both cases, the rotor lift converged within 4 revolutions. The unsteady fuselage drag has large 4/rev oscillations that are attributed to a pressure increase on the front of the fuselage when a rotor blades passes directly over the fuselage. A comparison of the fuselage drag between the α = -3° and -5° cases shows an increase in the amplitude of the drag for α = -5°. However, the mean drag coefficient for both α cases was 0.18, a 50% drag increase over the isolated fuselage mean C_D value of 0.12. The mean lift coefficient for the α = -3° case was -0.24, a 50% increase over the isolated fuselage value of -0.12. The lift for α = -5° in Fig. 24 is slowly increasing due to a low frequency oscillation seen in the fuselage lift.

Surface restricted streamlines and C_p contours for the baseline rotor/fuselage simulations are shown in Figs. 25 and 26 at three different blade azimuth angles for α =-3° and -5° respectively. These figures show that the flow separation, with respect to the slot locations, does not vary greatly from the baseline isolated fuselage cases. This indicates that the flow control slots do not need to be relocated for the rotor/fuselage case.

The baseline fuselage centerline C_p profiles are shown in Figs. 27-30 for the α = -3° and -5° rotor/fuselage cases. These figures show the C_p profiles for three blade azimuth angles of $\psi = 0°$, 30°, and 60°. The lower surface C_p profiles for both cases show little difference for the three rotor azimuth angles. The upper surface C_p profiles are similar between the $\psi = 30°$ and 60°, with the $\psi = 0°$ case having a higher pressure on the nose and tail as a result of the blade being directly over these regions. Therefore, most of the unsteady pressure forces are related to the passage of the rotor blades over the nose and tail section as expected. Comparing the lower surface C_p profiles between the α = -3° and -5° cases, shows the α = -3° case to have a larger suction peak on the ramp section with a higher pressure on the upper part of the ramp as compared to α = -5°. This higher pressure was also seen in the C_p surface contours in Figs. 25 and 26.

Rotor/Fuselage with Flow Control

Simulation of the rotor/fuselage with flow control was performed using the same slot location as in the isolated fuselage case. The ZNMF jets had a non-dimensional frequency of $F^+ = 0.56$, resulting in 4 blowing and suction cycles per rotor revolution. Slot heights of 0.0195" and 0.030" were evaluated for α = -3° with varying VR values, where the α = -5° was only evaluated using the 0.0195" slot height.

The fuselage unsteady drag and lift coefficients, as a function of the rotor azimuth angle, are given in Figs. 31-34 for α = -3° and -5°. These comparisons show that the flow control resulted in an overall drag decrease, shifting the baseline unsteady drag profile downward. Likewise, the

flow control resulted in an overall increase in the fuselage lift coefficient for α =-3° and a decrease for α = -5°.

The flow control performance of all of the CFD simulations are presented in Figs. 35-38. The flow control performance for the two jet slot heights at α = -3° are shown in Fig. 35. These results show that the two slot heights for the same C_μ value, only have a small difference with the larger 0.030" slot having slightly improved performance. A comparison of the two slots for the fuselage lift in Fig. 36, show the larger slot performing approximately 5% better than the smaller slot. Therefore, the flow control performance for the fuselage drag shows an expected dependence on C_μ, while the lift indicates a dependence on the slot height and C_μ.

The percentage change of C_D and C_L from the baseline cases for increasing C_μ are presented in Figs. 37 and 38. The percentage mean drag change in Fig. 37 indicates that the isolated fuselage and rotor/fuselage for α = -3°, have a similar percentage drag reduction from their respective baseline values. The α = -5° performance results for the isolated fuselage and the rotor/fuselage cases are not similar as was seen for the α = -3° case.

The fuselage lift performance in Fig. 38 indicates that both the isolated fuselage and rotor/fuselage simulations initially show an increase in lift on the fuselage for increasing C_μ at the α = -3° condition. The isolated fuselage lift shows a decrease as C_μ increases from 0.0045 to 0.0080, whereas the lift for the rotor/fuselage simulation continues to increase. The α = -5° fuselage flow control case for the rotor/fuselage simulation has an initial decrease of fuselage lift as C_μ increases. The lift performance then recovers as C_μ is increased further from 0.0045 to 0.0120, approaching the original baseline lift value. The isolated fuselage lift results are significantly different from the rotor/fuselage simulations at α =-5° showing a much larger percentage download increase from the baseline for increasing C_μ.

The effect of the flow control on the ramp surface pressure can be seen in Figs. 39 and 40 for the 0.0195" slot height and VR = 1.86. These two figures show the ramp region for three different blade azimuth angles. Overall, the surface C_p contours show an increase of the ramp base pressure with AFC, reducing fuselage drag. The flow separation locations have also moved inward with a larger suction pressure on the edges of the ramp region, contributing to an increase in fuselage drag.

A comparison of the spanwise surface C_p values halfway up the ramp, on a constant z/R_F = -0.075 plane, are made in Figs. 41 and 42 for both the α = -3° and -5° rotor/fuselage cases. The instantaneous C_p plots are given for $\psi = 0°$, 30°, and 60°. A comparison of the baseline C_p values for both cases reveals similar pressure profiles for the three blade azimuth angles where the α = -5° baseline case has a slightly higher base pressure than the α = -3° baseline case. The C_p profiles with AFC, for both α cases, have an increase in the ramp base pressure with an increase of the suction pressure on the corners.

Figures 43 and 44 compare the lower surface centerline C_p profiles for the baseline and flow control cases for the two angle-of-attack cases at an azimuth angle of $\psi = 0°$, which is characteristic of the other blade azimuth angles. The upper C_p centerline profile was not effected by the flow control, however flow control did modify the lower centerline C_p profile near the ramp region. Both α cases show an increase in the suction pressure and higher ramp base pressure with AFC.

A view of the fuselage and rotor wakes are presented in Figs. 45-48 for the baseline and flow controlled CFD simulations showing iso-surface contours of the Q-criterion shaded by C_p. Figures 45 and 46 show the rotor tip vortices and the juncture vortex from the upper pylon. Figures 47 and 48 are side views of the simulation, highlighting the interaction of the rotor wake vorticity with the fuselage. This view indicates that there is little interaction of the rotor wake vorticity with fuselage ramp region at this forward flight condition. It also shows the trajectory of the juncture vortex on the side of the fuselage, entering the ramp region. The side view highlights the modification of the wake from the separated flow on the ramp and unsteadiness of the streamwise vortex from the ramp region.

Summary

This investigation explores the effectiveness of flow control for rotorcraft fuselage drag reduction using ZNMF jets. This research extends the isolated fuselage work of Schaeffler et al. (Ref. 10) to a more relevant environment by including a rotor. This effort is also complementary to a future 1/3 scaled rotor/fuselage wind tunnel experiment planned at the NASA 14-by 22-Foot Subsonic Tunnel. The outcome of this numerical investigation will be used as guidance for the design of a fuselage flow controlled model for the future test.

The isolated fuselage simulation used the same fuselage geometry as in the previous investigation of Schaeffler et al. (Ref. 10) with the addition of an upper pylon that partially encloses the rotor shaft. It was discovered that the inclusion of the upper pylon at α = -3° resulted in a juncture vortex that interacted with the separated flow in the ramp region. This interaction of the juncture vortex with the ramp resulted in unsteady vortex shedding from the ramp, increasing the fuselage drag by 20%. The isolated fuselage was simulated at a typical long range cruise condition were $M_\infty = 0.209$ with the fuselage at α = -3°. A RANS simulation of the isolated fuselage with flow control resulted in a 17% drag reduction from the baseline with a 7% decrease of the fuselage download force. The flow control at this condition had a slot height of 0.0195" and a peak jet VR of 2.0, resulting in a C_μ value of 0.008. At α = -5°, the flow control resulted in a drag increase. However, a

marginal drag reduction of 2% was seen for a very large C_μ value of 0.015. In addition to the drag increase, the fuselage download also increased dramatically for the -5° flow control case by 140% for $C_\mu = 0.0069$. The flow control for the α = -5° case resulted in lower pressures on the bottom ramp corner and the bottom of the tail boom, as compared to the baseline pressure. These low pressure regions were identified as the source of the increase fuselage download.

Including the rotor in the numerical simulations introduced a large 4/rev oscillation of the fuselage forces, increasing the mean fuselage drag by 50% with a 50% increase of the fuselage download as compared to the isolated fuselage at α = -3°. Turning on the fuselage flow control, for the 0.0195" slot with a jet VR of 1.86 (C_μ=0.0069), resulted in a 17% drag reduction with a 22% reduction of the fuselage download force. The reduction of the fuselage download has a compounding positive effect on the overall vehicle performance, since the rotor thrust can be reduced, which further reduces the download on the fuselage. Evaluation of two different flow control jet slot heights of 0.0195" and 0.030" resulted in similar drag performance curves when plotted as a function of C_μ. These result indicated that the performance of the flow control for this configuration is a function of the jet momentum coefficient, C_μ.

Comparing the flow control performance between the isolated fuselage and rotor/fuselage simulations at α = -3° showed that the drag performance, in terms of percentage drag reduction, was similar over the range of C_μ evaluated. Unfortunately, this was not the case for α = -5°, where the isolated fuselage, unlike the rotor/fuselage case, had an initial drag increase with increasing flow control C_μ and a significantly larger increase of the fuselage download.

Acknowledgments

The authors thank the Subsonic Rotary Wing (SRW) Project of NASA's Fundamental Aeronautics Program for supporting this work. Dr. Doug Boyd from NASA Langley for his help and guidance on using CAMRAD II and coupling it with the OVERFLOW flow solver. Dr. Peter Buning from NASA Langley for his continuing development of the OVERFLOW code, making these simulations possible. Preston Martin and Oliver Wong from U.S. Army AFDD for providing the rotor properties and discussion of results. Computations were performed on the NAS Pleiades machine and on the K machine at NASA Langley. Thanks to all of the people who support and keep these machines operational.

References

[1]Leishman, J. G., *Principles of Helicopter Aerodynamics*, Cambridge University Press, second edition, 2006.

[2]Gatard, J., Costes, M., Kroll, N., Renzoni, P., Kokkalis, A., Rocchetto, A., Serr, C., Larrey, E., Filippone, A., and Wehr, D., "High Reynolds Number Helicopter Fuselage Test in the ONERA F1 Pressureized Wind Tunnel," 23rd European Rotorcraft Forum Paper 167, Dresden, Germany, September 16-18, 1997.

[3]Martin, P., Tung, C., Hassan, A., Cerchie, D., and Roth, J., "Active Flow Control Measurements and CFD on a Transport Helicopter Fuselage," American Helicopter Society 61st Annual Forum, Grapevine, TX, 2005.

[4]Ben-Hamou, E., Arad, E., and Seifert, A., "Generic Transport Aft-Body Drag Reduction using Active Flow Control," AIAA Paper 2004-2509, 2004.

[5]Freeman, C. and Mineck, R. E., "Fuselage Surface Pressure Measurments of a Helicopter Wind-Tunnel Model with a 3.15-meter Diameter Single Rotor," NASA TM 80051, Langley Research Center, March 1979.

[6]Phelps, A. E. and Berry, J. D., "Description of the U. S. Army Small-Scale 2-Meter Rotor Test System," NASA TM 87762 (AVSCOM TM-86-B-4), Langley Research Center, February 1987.

[7]Mineck, R. and Gorton, S. A., "Steady and Periodic Pressure Measurements on a Generic Helicopter Fuselage Model in the Presence of a Rotor," NASA TM 2000-210286, Langley Research Center, June 2000.

[8]Renaud, T., O'Brien, D., Smith, M., and Potsdam, M., "Evaluation of Isolated Fuselage and Rotor-Fuselage Interaction Using CFD," American Helicopter Society 60th Annual Forum, Baltimore, MD, June 2004.

[9]O'Brien, D. M. and Smith, M. J., "Analysis of Rotor-Fuselage Interactions Using Various Rotor Models," AIAA Paper 2005-0468, January 2005.

[10]Schaeffler, N. W., Allan, B. G., Lienard, C., and Le Pape, A., "Progress Towards Fuselage Drag Reduction via Active Flow Control: A Combined CFD and Experimental Effort," 36^{th} European Rotorcraft Forum Paper 064, Paris, France, September 2010.

[11]Buning, P. G., Jespersen, D. C., Pulliam, T. H., Klopfer, W. M., Chan, W. M., Slotnick, J. P., Krist, S. E., and Renze, K. J., "OVERFLOW User's Manual Version 1.8m," Technical report, NASA Langley Research Center, 1999.

[12]Jespersen, D., Pulliam, T., and Buning, P., "Recent Enhancements to OVERFLOW," AIAA paper 97–0644, January 1997.

[13]Pulliam, T. H. and Chaussee, D. S., "A Diagonal Form of an Implicit Approximate-Factorization Algorithm," *Journal of Computational Physics*, Vol. 39, February 1981, pp. 347–363.

[14]Steger, J. L., Dougherty, F. C., and Benek, J. A., "A Chimera Grid Scheme," Advances in Grid Generation, edited by K. N. Ghia and U. Ghia, Vol. 5, FED, 1983.

[15]Murphy, K., Buning, P., Pamadi, B., Scallion, W., and Jones, K., "Status of Stage Separation Tool Development for Next Generation Launch Technologies," AIAA Paper 2004-2595, June 2004.

[16]Spalart, P. and Allmaras, S. R., "One-Equation Turbulence Model for Aerodynamic Flows," AIAA Paper 1992-0439, 1992.

[17]Menter, R. F., "Two-Equation Eddy-Viscosity Turbulence Models for Engineering Applications," *AIAA Journal*, Vol. 32, (8), 1994, pp. 1598–1605.

[18]Shur, M., Strelets, M., Travin, A., and Spalart, P., "Turbulence Modeling in Rotating and Curved Channels: Assessing the Spalart-Shur Correction," *AIAA Journal*, Vol. 38, (5), May 2000, pp. 784–792.

[19]Wong, O. D., Noonan, K. W., Watkins, A. N., Jenkins, L. N., and Yao, C. S., "Non-Intrusive Measurements of a Four-Bladed Rotor in Hover - A First Look," American Helicopter Society Specialist Conference, San Francisco, CA, January 2010.

[20]Johnson, W., "Rotorcraft Aerodynamics Models for a Comprehensive Analysis," 54th Annual American Helicopter Society Forum, January 1998.

[21]Johnson, W., "CAMRAD II Comprehensive Analytical Model of Rotorcraft Aerodynamics and Dynamics," Johnson Aeronautics, Palo Alto, Califorinia, 2005.

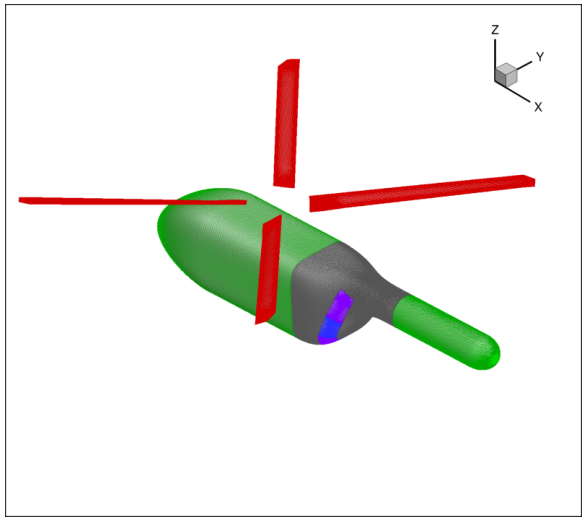

Fig. 1. Surface grids on the fuselage and rotor.

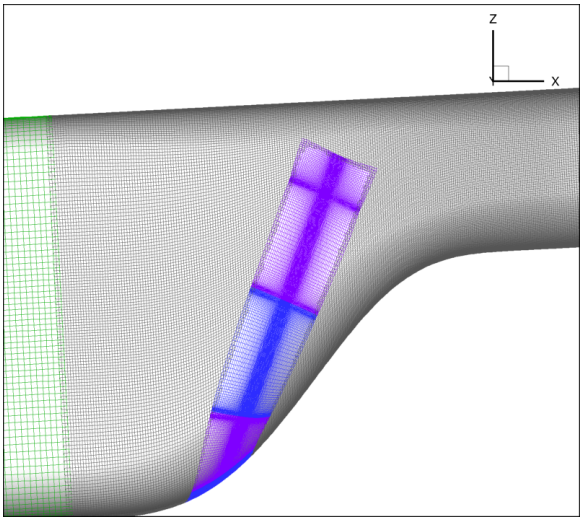

Fig. 2. Detail of grids used for flow control slots.

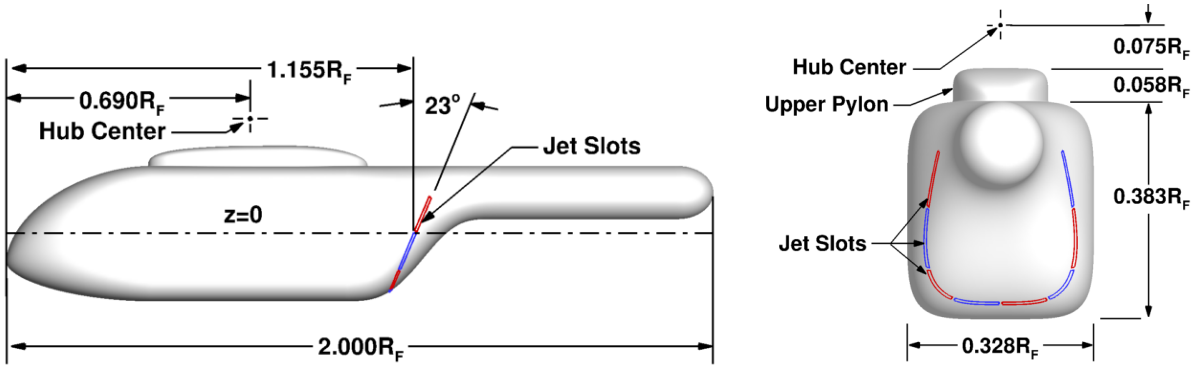

Fig. 3. Fuselage geometry and slot locations used for the CFD simulations where R_F is 61.9655 for the 1/3 scale 14- by 22-foot Subsonic Wind Tunnel model

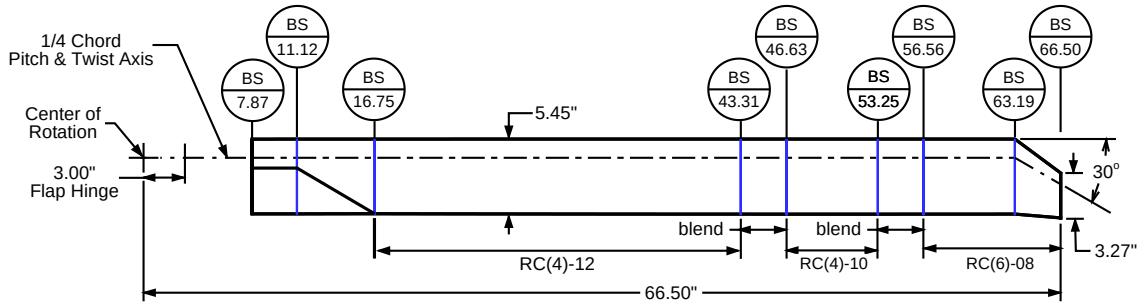

Fig. 4. Blade layout.

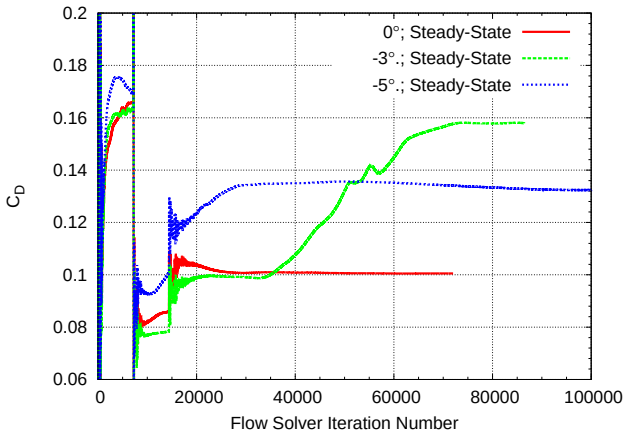

Fig. 5. Isolated fuselage baseline drag coefficient convergence history for steady-state solution.

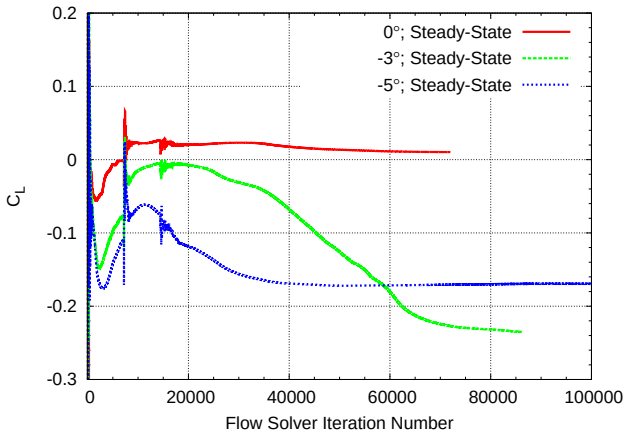

Fig. 6. Isolated fuselage baseline lift coefficient convergence history for steady-state solution.

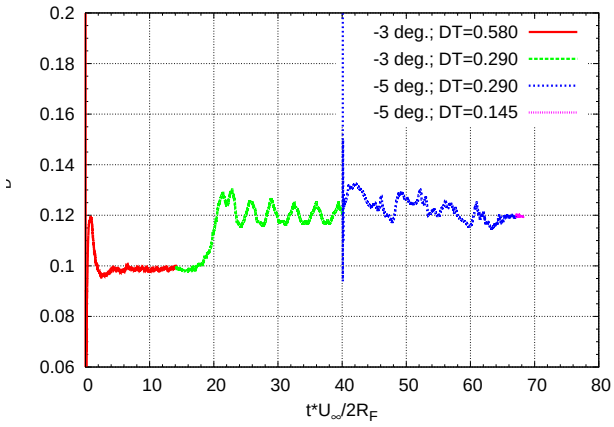

Fig. 7. Drag coefficient history for the time-accurate simulation of the baseline isolated fuselage for α = -3° and -5°.

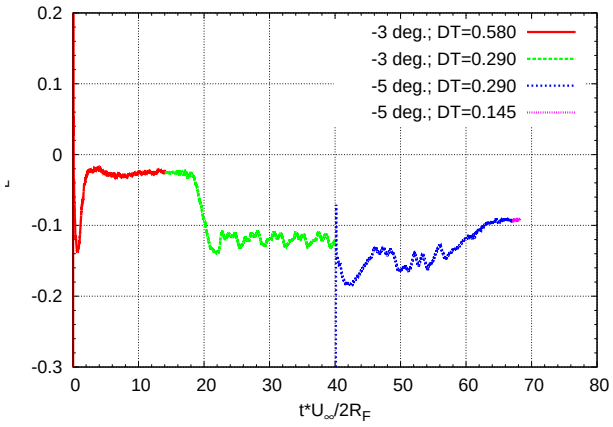

Fig. 8. Lift coefficient history for the time-accurate simulation of the baseline isolated fuselage for α = -3° and -5°.

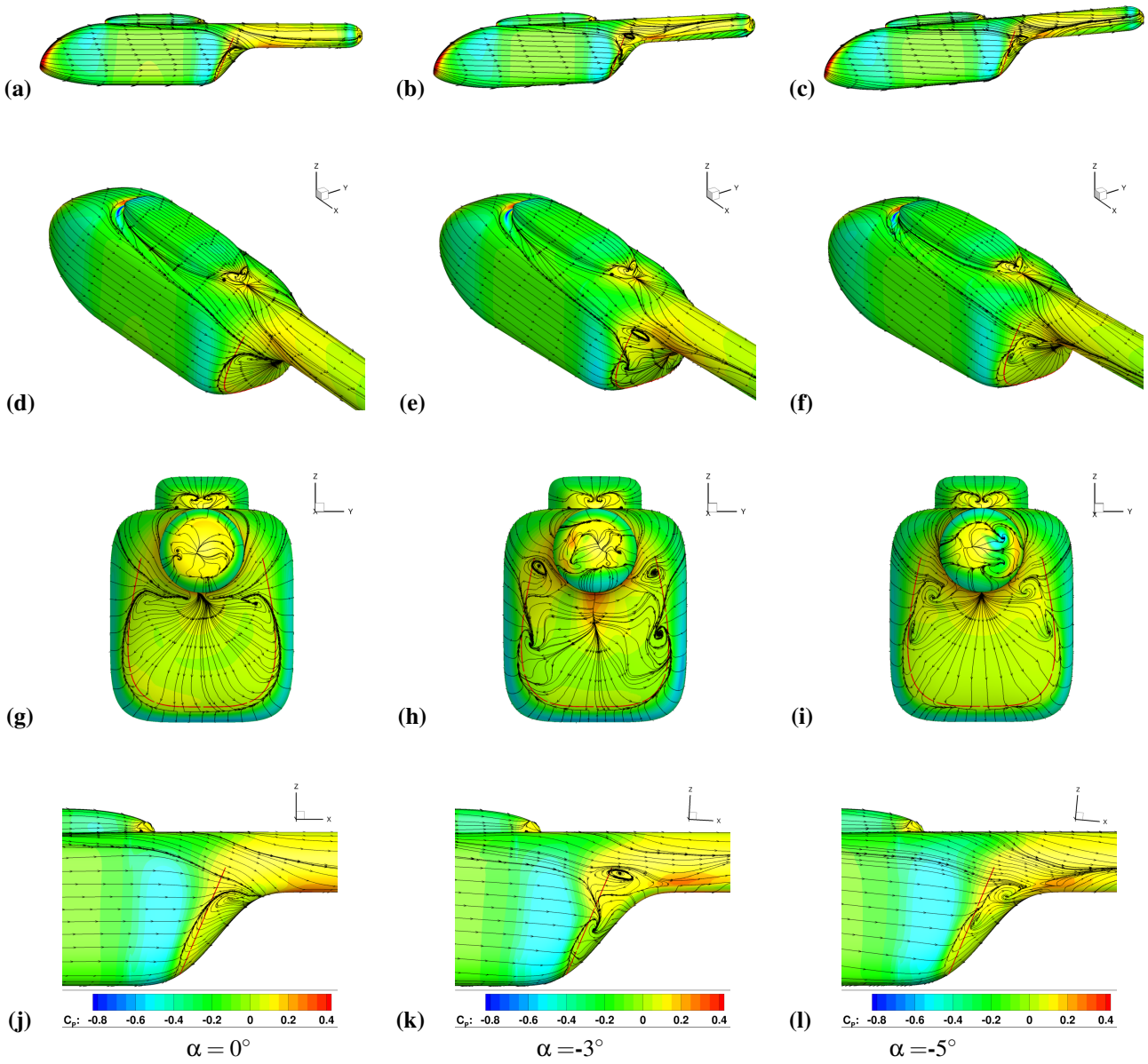

Fig. 9. Baseline fuselage for M_∞=0.2093 at $\alpha = 0°$, -3°, and -5° shaded by the surface C_p with surface restricted streamlines and flow control slots outlined in red: (a-c) side view, (d-f) view showing juncture vortex from upper pylon interacting with ramp (g-i) rear view of ramp region (j-l) close-up of the side view.

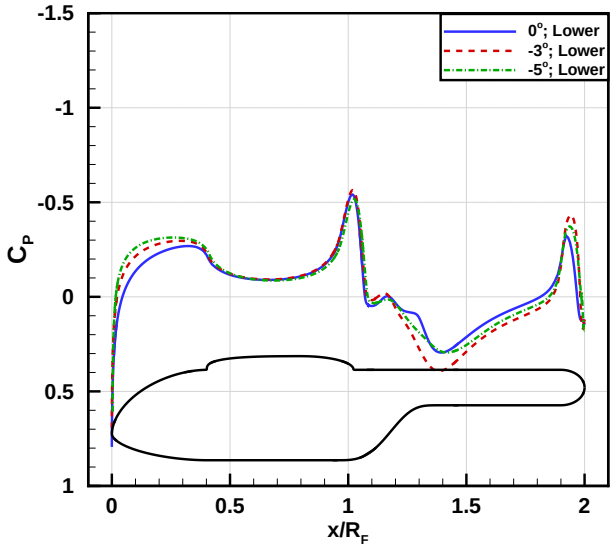

Fig. 10. Fuselage centerline C_p values for the isolated fuselage lower surface at $\alpha = 0°$, -3°, and -5°.

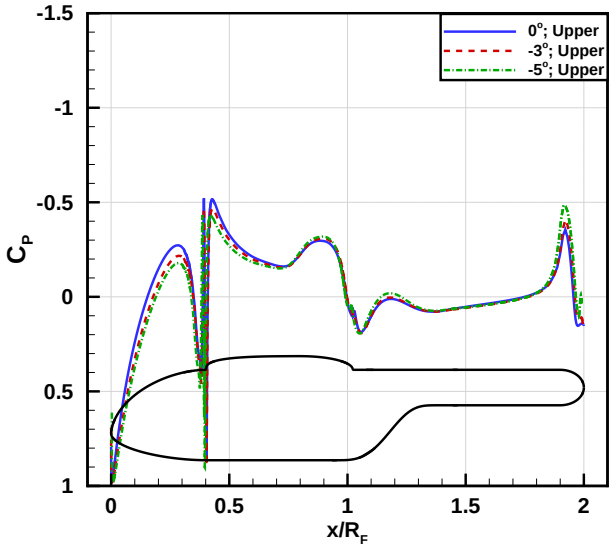

Fig. 11. Fuselage centerline C_p values for the isolated fuselage upper surface at $\alpha = 0°$, -3°, and -5°.

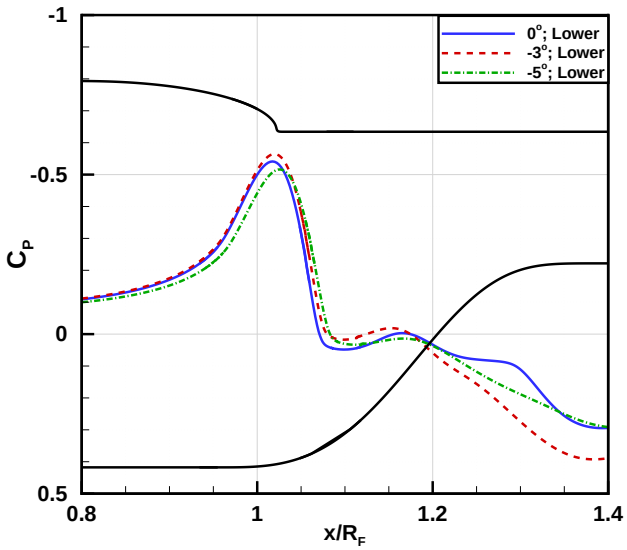

Fig. 12. Fuselage centerline C_p values for the isolated fuselage lower surface at $\alpha = 0°$, -3°, and -5°

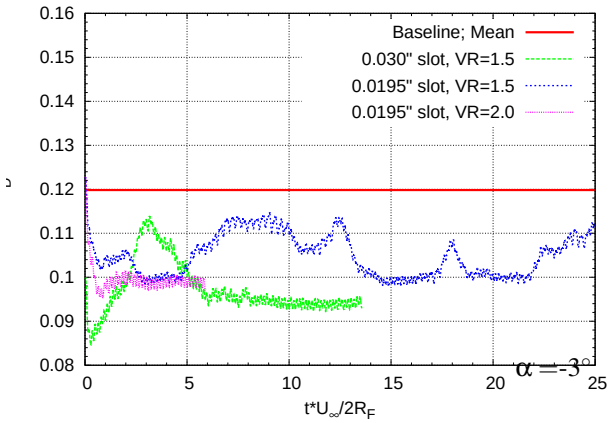

Fig. 13. Drag coefficient history for the time-accurate simulation of the isolated fuselage with ZNMF control jets for $\alpha = -3^{\circ}$. All simulations are using a jet blowing frequency of $F^{+} = 0.56$.

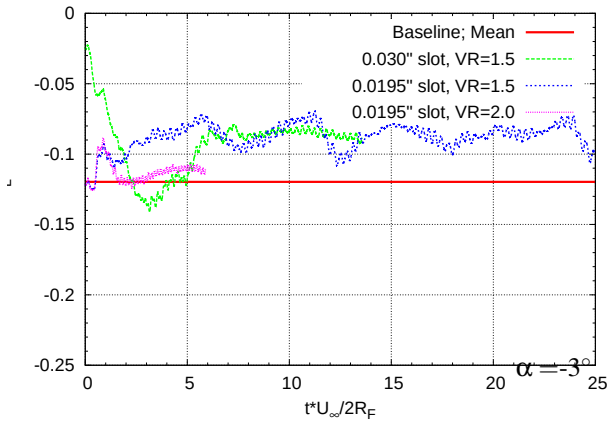

Fig. 14. Lift coefficient history for the time-accurate simulation of the isolated fuselage with ZNMF control jets for $\alpha = -3^{\circ}$. All simulations are using a jet blowing frequency of $F^{+} = 0.56$.

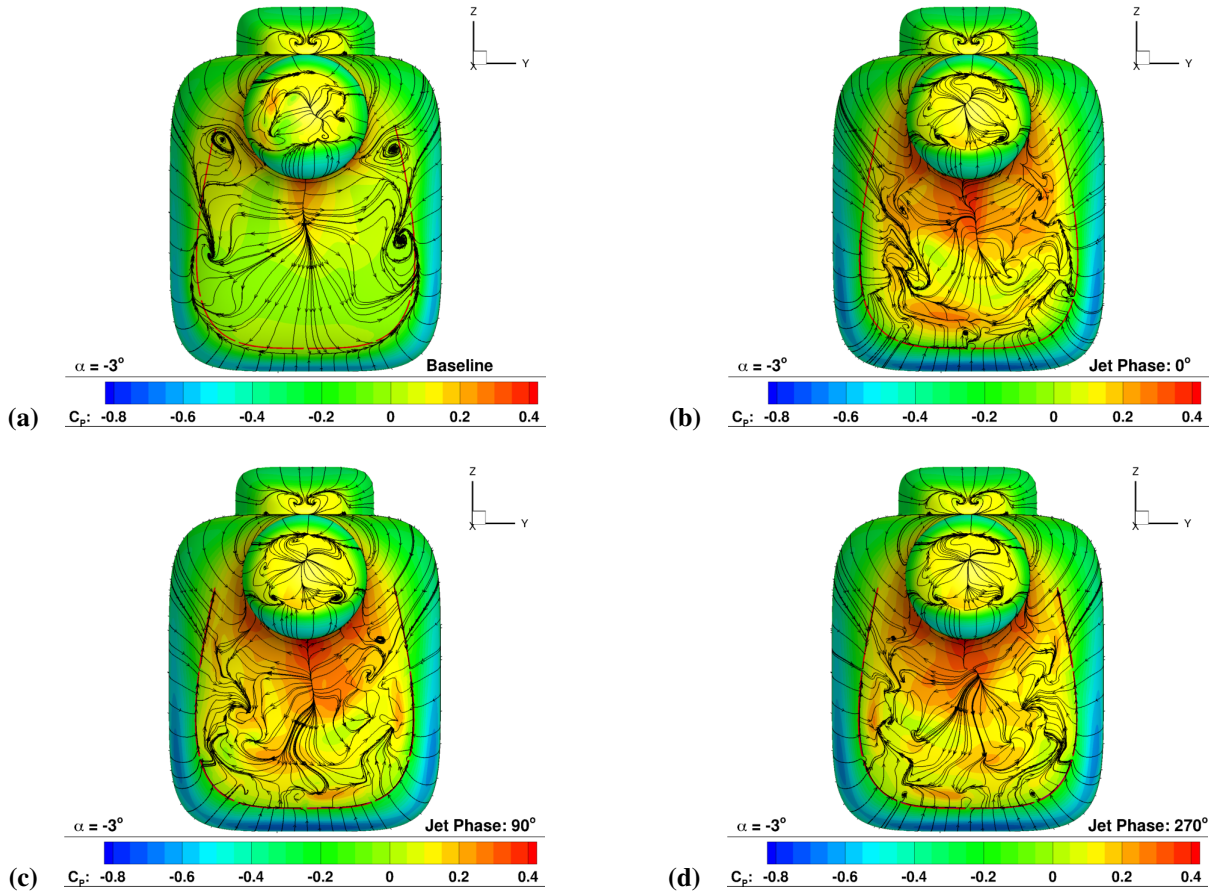

Fig. 15. Comparison of the C_p contours and surface restricted streamlines on the ramp region for the isolated fuselage at $\alpha = -3^{\circ}$ for (a) the baseline case (i.e. no flow control) and AFC case at three actuator phases, (b) $\phi = 0^{\circ}$, (c) $\phi = 90^{\circ}$, and (d) $\phi = 270^{\circ}$ for a VR = 2.0.

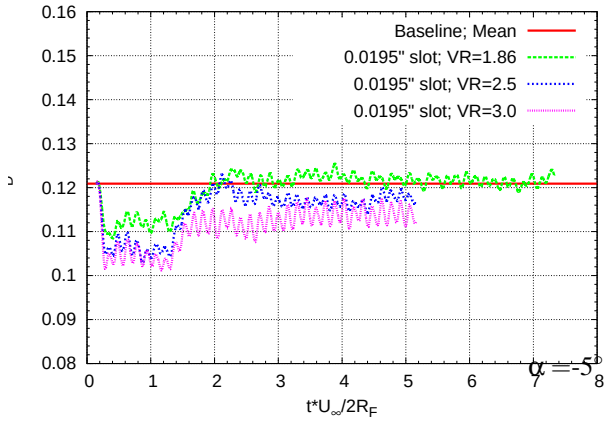

Fig. 16. Drag coefficient history for the time-accurate simulation of the isolated fuselage with ZNMF control jets for $\alpha = -5^{\circ}$. All simulations are using a jet blowing frequency of $F^{+} = 0.56$.

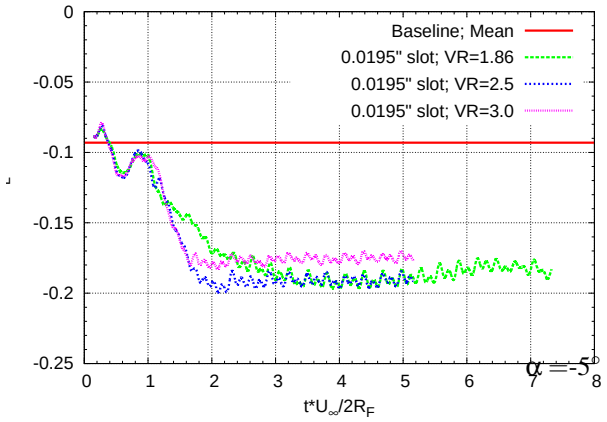

Fig. 17. Lift coefficient history for the time-accurate simulation of the isolated fuselage with ZNMF control jets for $\alpha = -5^{\circ}$. All simulations are using a jet blowing frequency of $F^{+} = 0.56$.

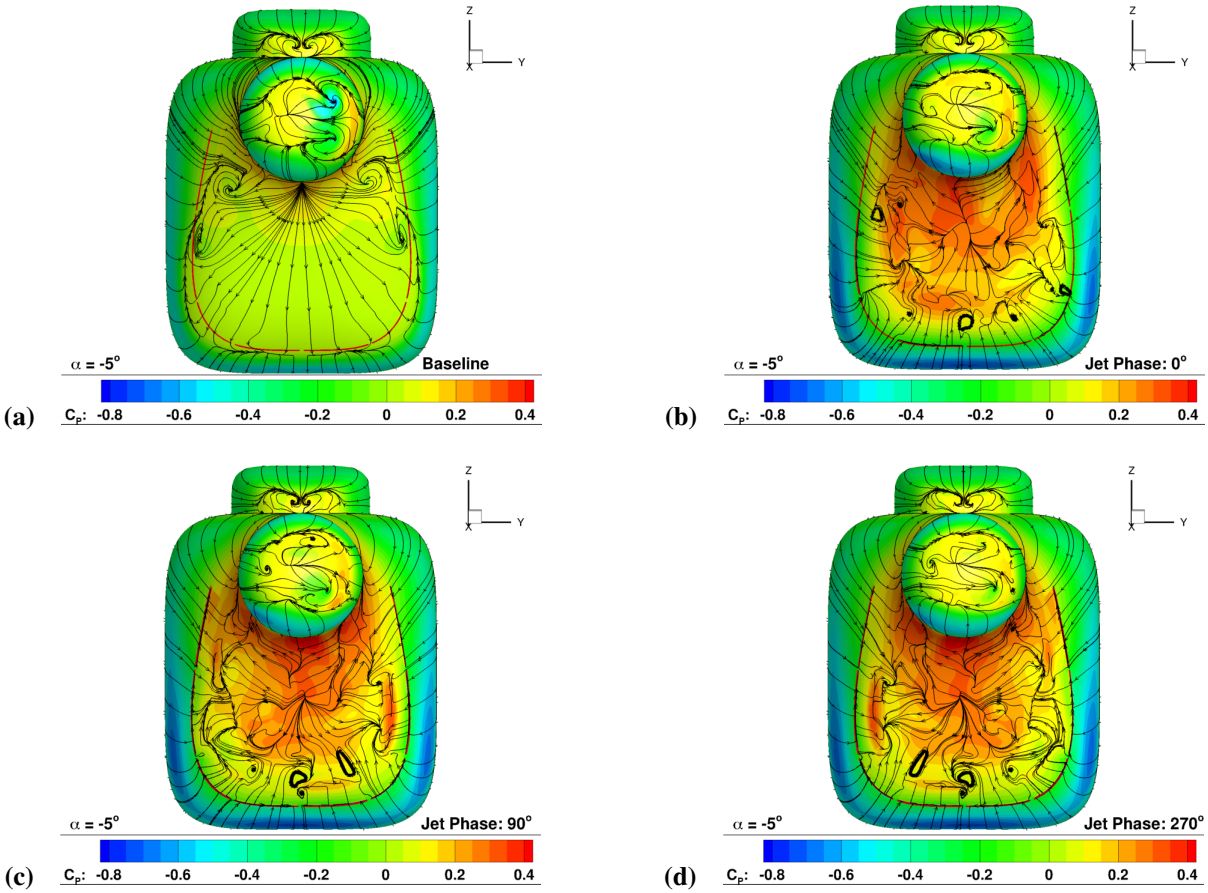

Fig. 18. Comparison of the C_p contours and surface restricted streamlines on the ramp region for the isolated fuselage at $\alpha = -5^{\circ}$ for (a) the baseline case (i.e. no flow control) and AFC case at three actuator phases, (b) $\phi = 0^{\circ}$, (c) $\phi = 90^{\circ}$, and (d) $\phi = 270^{\circ}$ for a VR = 2.5.

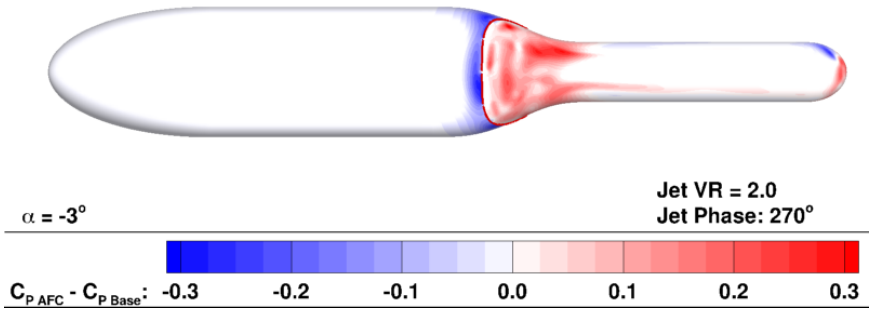

Fig. 19. Bottom view of the computed C_p difference between the baseline and AFC isolated fuselage at $\alpha = -3^\circ$ case.

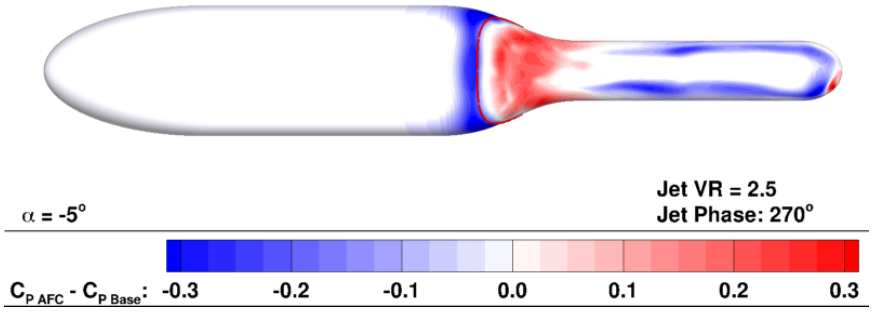

Fig. 20. Bottom view of the computed C_p difference between the baseline and AFC isolated fuselage at $\alpha = -5^\circ$ case.

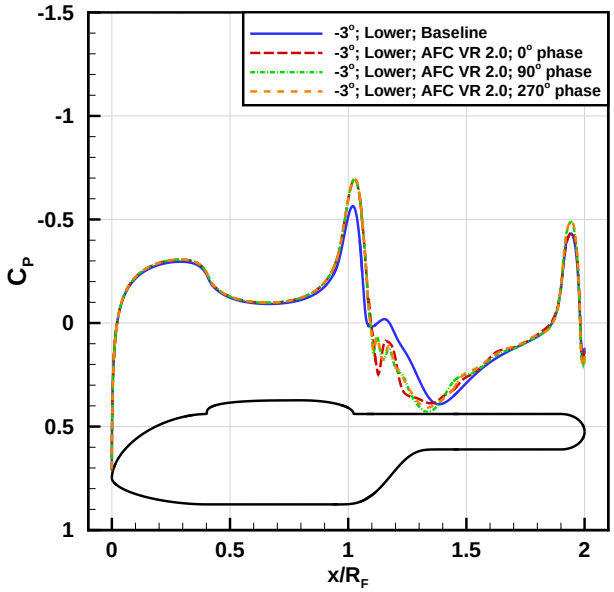

Fig. 21. Fuselage centerline C_p values for the isolated fuselage lower surface at $\alpha = -3^\circ$ for the baseline and flow control cases.

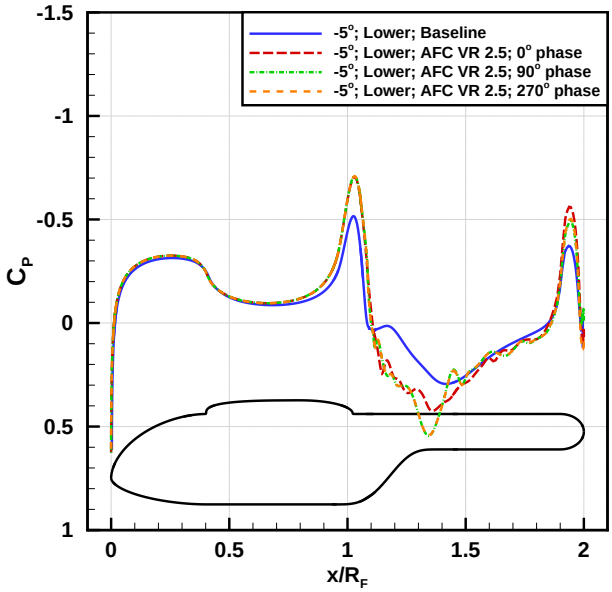

Fig. 22. Fuselage centerline C_p values for the isolated fuselage upper surface at $\alpha = -5^\circ$ for the baseline and flow control cases.

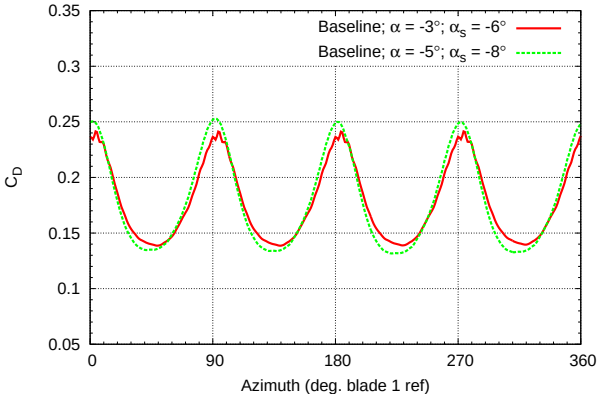

Fig. 23. Baseline fuselage drag coefficient for the rotor/fuselage simulation at $\alpha = -3^\circ$ and -5° with $M_\infty = 0.209$, and $CT/\sigma = 0.08$.

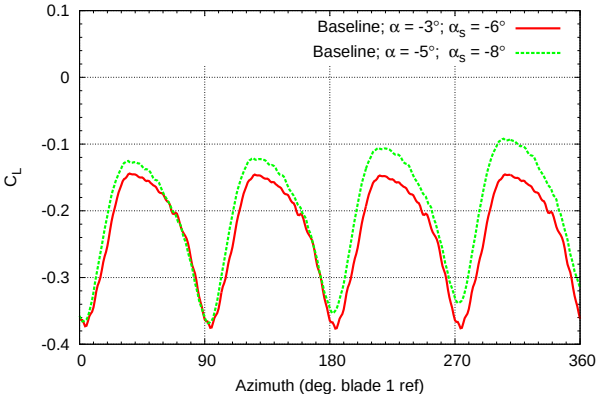

Fig. 24. Baseline fuselage lift coefficient for the rotor/fuselage simulation at $\alpha = -3^\circ$ and -5° with $M_\infty = 0.209$, and $CT/\sigma = 0.08$.

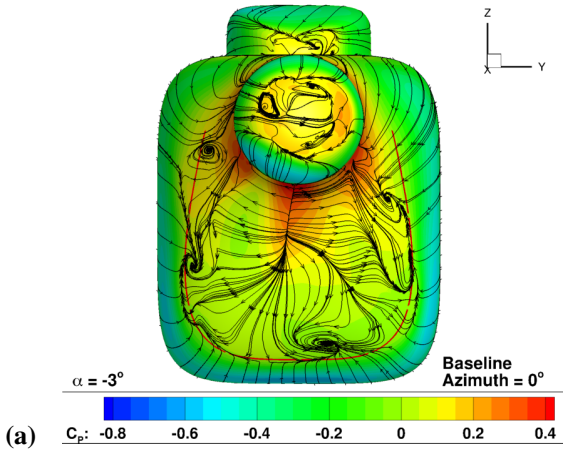

(a)

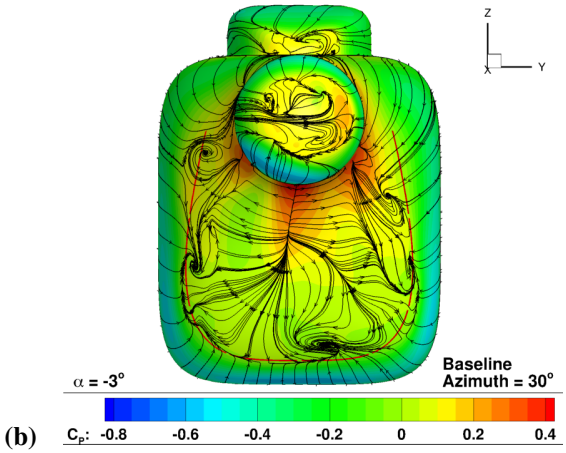

(b)

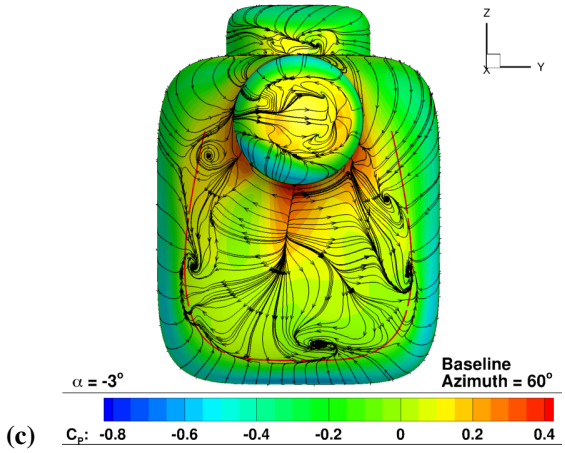

(c)

Fig. 25. Rear ramp view of the baseline rotor/fuselage simulation for the α = -3° case. Surface C_p contours with surface restricted streamlines at (a) $\psi = 0°$, (b) $\psi = 30°$, and (c) $\psi = 60°$. (Simulation parameters: $\mu = 0.35$, $CT/\sigma = 0.08$, M_∞=0.2093)

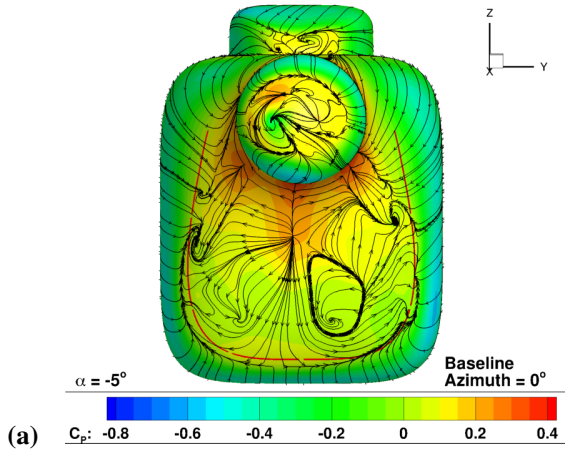

(a)

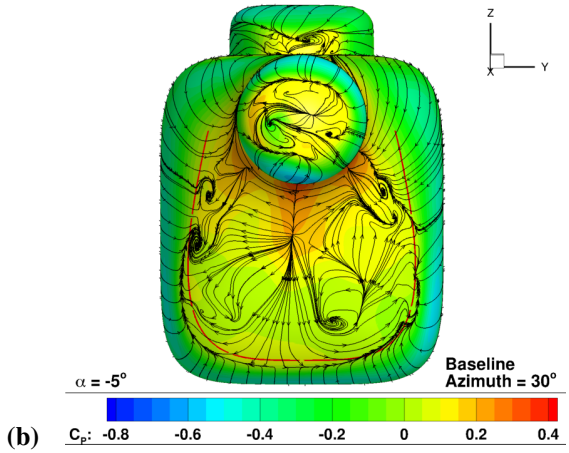

(b)

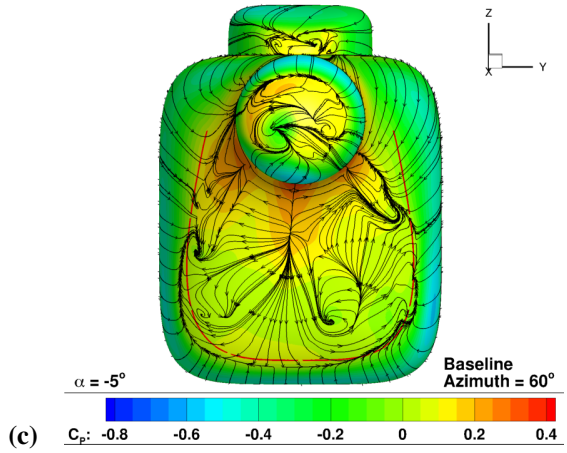

(c)

Fig. 26. Rear ramp view of the baseline rotor/fuselage simulation for the α = -5° case. Surface C_p contours with surface restricted streamlines at (a) $\psi = 0°$, (b) $\psi = 30°$, and (c) $\psi = 60°$. (Simulation parameters: $\mu = 0.35$, $CT/\sigma = 0.08$, M_∞=0.2093)

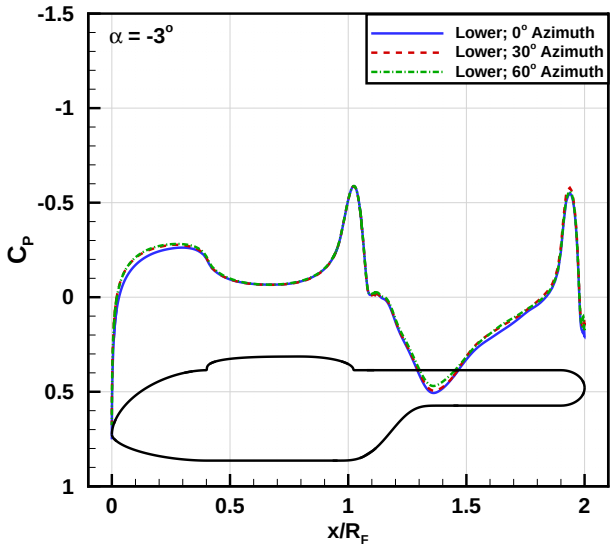

Fig. 27. Lower fuselage centerline C_p values for the baseline rotor/fuselage simulation at $\alpha = -3^\circ$ for varying rotor azimuth angles.

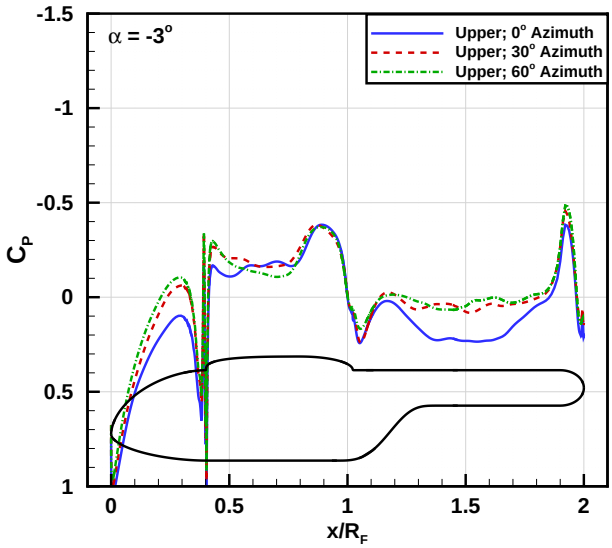

Fig. 28. Upper fuselage centerline C_p values for the baseline rotor/fuselage simulation at $\alpha = -3^\circ$ for varying rotor azimuth angles.

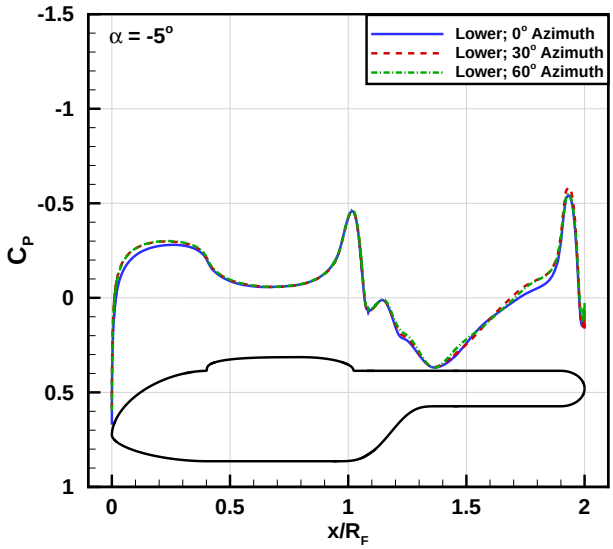

Fig. 29. Lower fuselage centerline C_p values for the baseline rotor/fuselage simulation at $\alpha = -5^\circ$ for varying rotor azimuth angles.

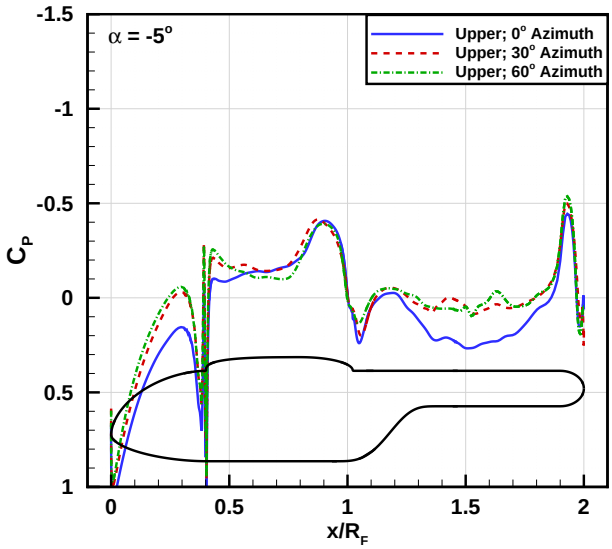

Fig. 30. Upper fuselage centerline C_p values for the baseline rotor/fuselage simulation at $\alpha = -5^\circ$ for varying rotor azimuth angles.

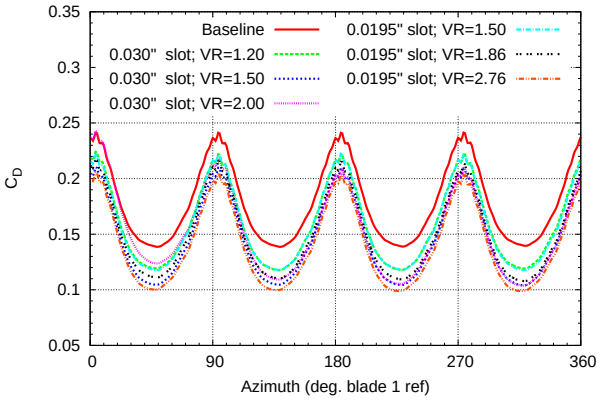

Fig. 31. Unsteady fuselage drag coefficient of the rotor/fuselage simulations at α = -3° for varying jet VR values. (Simulation parameters: $F^+ = 0.56$, $\mu = 0.35$, $CT/\sigma = 0.08$, M_∞=0.2093)

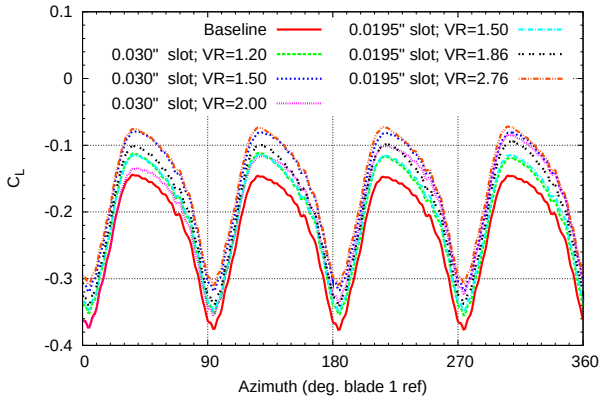

Fig. 32. Unsteady fuselage lift coefficient of the rotor/fuselage simulations at α = -3° for varying jet VR values. (Simulation parameters: $F^+ = 0.56$, $\mu = 0.35$, $CT/\sigma = 0.08$, M_∞=0.2093)

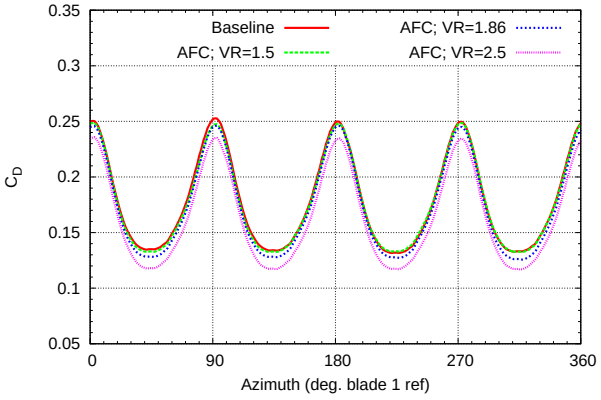

Fig. 33. Unsteady fuselage drag coefficient of the rotor/fuselage simulations at α = -5° for varying jet VR values. (Simulation parameters: $F^+ = 0.56$, $\mu = 0.35$, $CT/\sigma = 0.08$, M_∞=0.2093)

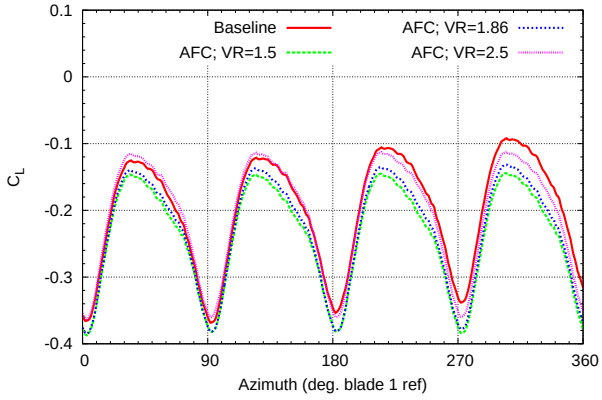

Fig. 34. Unsteady fuselage lift coefficient of the rotor/fuselage simulations at α = -5° for varying jet VR values. (Simulation parameters: $F^+ = 0.56$, $\mu = 0.35$, $CT/\sigma = 0.08$, M_∞=0.2093)

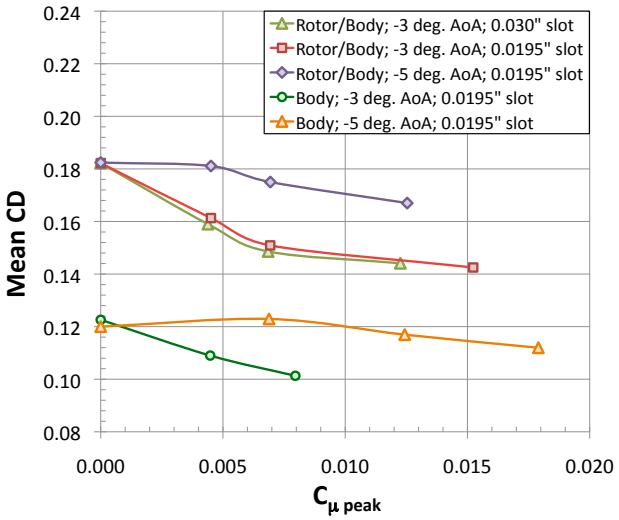

Fig. 35. Mean fuselage drag coefficient as a function of C_μ for the isolated fuselage and rotor/fuselage CFD simulations.

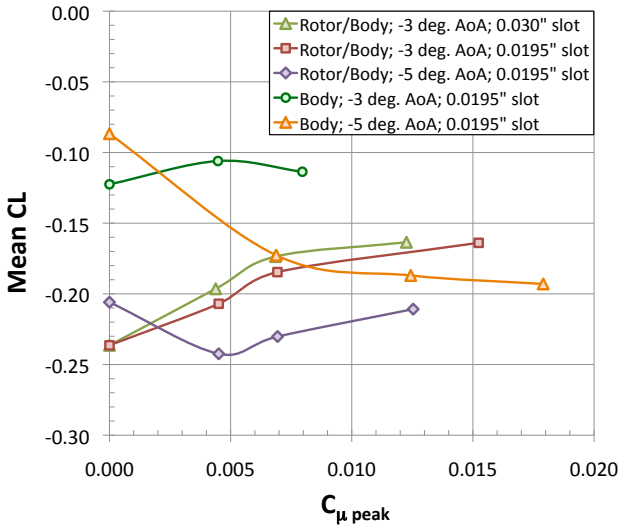

Fig. 36. Mean fuselage lift coefficient as a function of C_μ for the isolated fuselage and rotor/fuselage CFD simulations

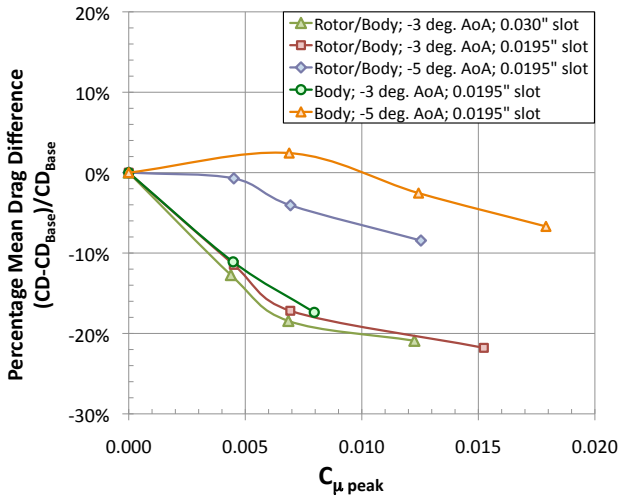

Fig. 37. Percentage change in the mean fuselage drag coefficient as a function of C_μ for the isolated fuselage and rotor/fuselage CFD simulations.

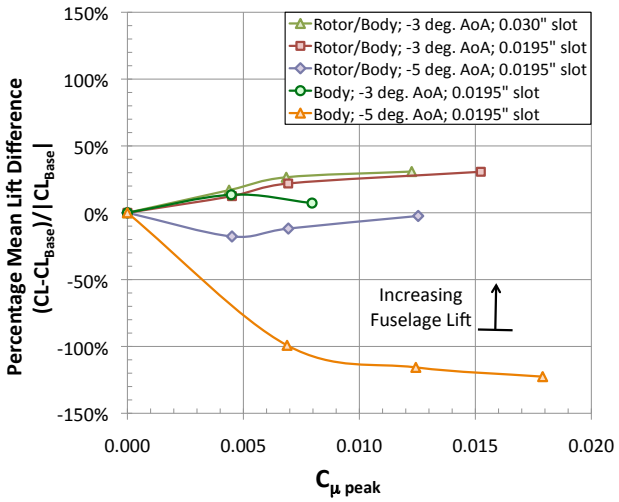

Fig. 38. Percentage change in the mean fuselage lift coefficient as a function of C_μ for the isolated fuselage and rotor/fuselage CFD simulations.

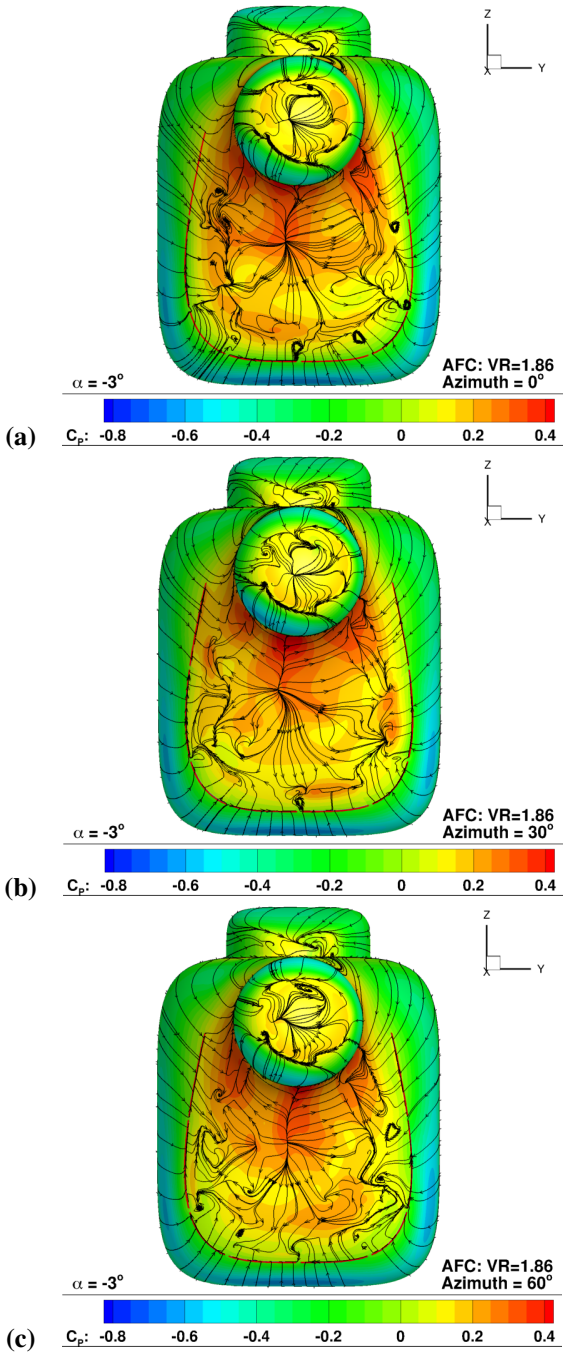

Fig. 39. Rear ramp view of the baseline rotor/fuselage simulation for α = -3°. Surface C_p contours with surface restricted streamlines at (a) $\psi = 0°$, (b) $\psi = 30°$, and (c) $\psi = 60°$. (Simulation parameters: VR=1.86, h = 0.0195", C_μ = 0.0069, $\mu = 0.35$, $CT/\sigma = 0.08$, M_∞=0.2093)

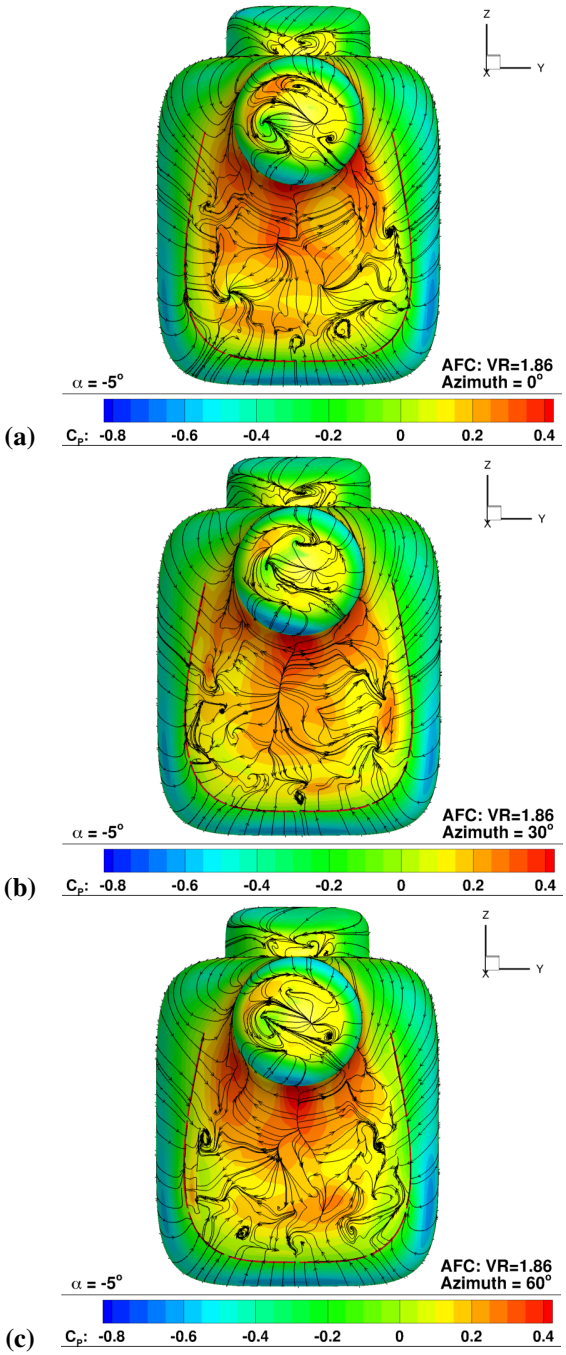

Fig. 40. Rear ramp view of the baseline rotor/fuselage simulation for α = -5°. Surface C_p contours with surface restricted streamlines at (a) $\psi = 0°$, (b) $\psi = 30°$, and (c) $\psi = 60°$. (Simulation parameters: VR=1.86, h = 0.0195", C_μ = 0.0069, $\mu = 0.35$, $CT/\sigma = 0.08$, M_∞=0.2093)

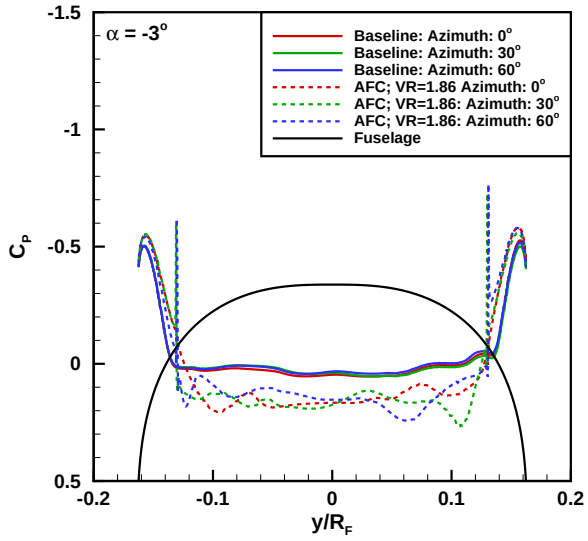

Fig. 41. Spanwise surface C_p on the ramp for the baseline and AFC cases at $\alpha = -3^\circ$.

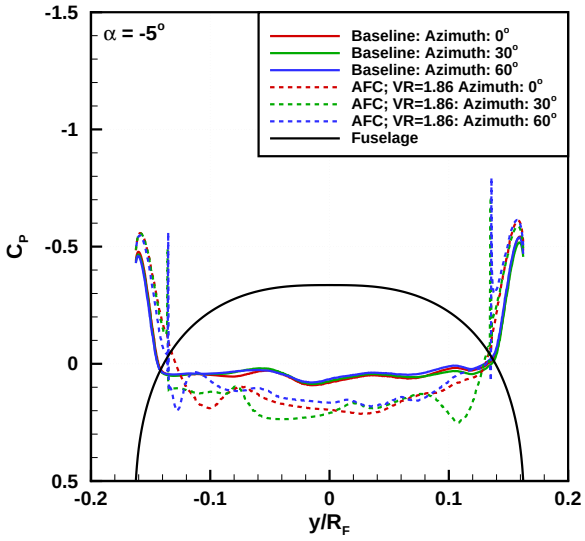

Fig. 42. Spanwise surface C_p on the ramp for the baseline and AFC cases at $\alpha = -5^\circ$.

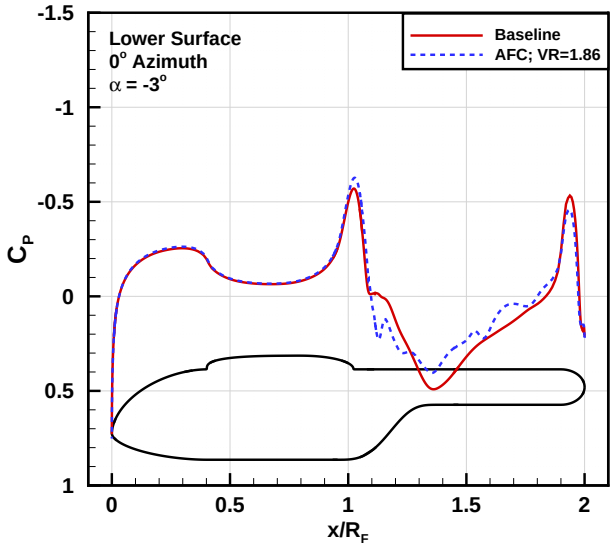

Fig. 43. Fuselage centerline C_p values for the rotor/fuselage simulation at $\alpha = -3^\circ$ comparing the baseline and AFC cases.

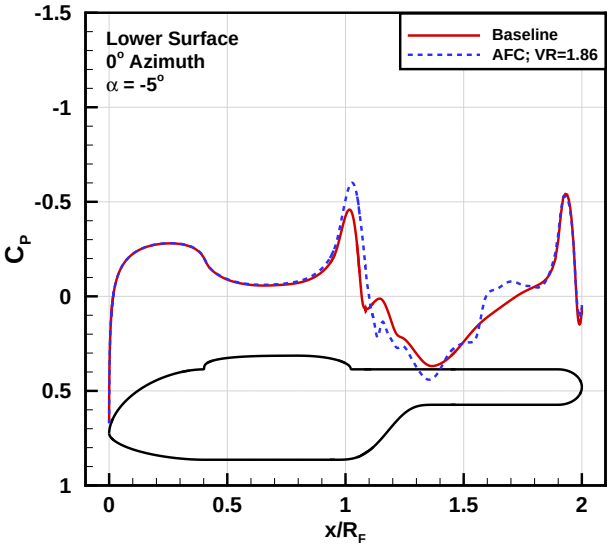

Fig. 44. Fuselage lower centerline C_p values for the rotor/fuselage simulation at $\alpha = -5^\circ$ comparing the baseline and AFC cases.

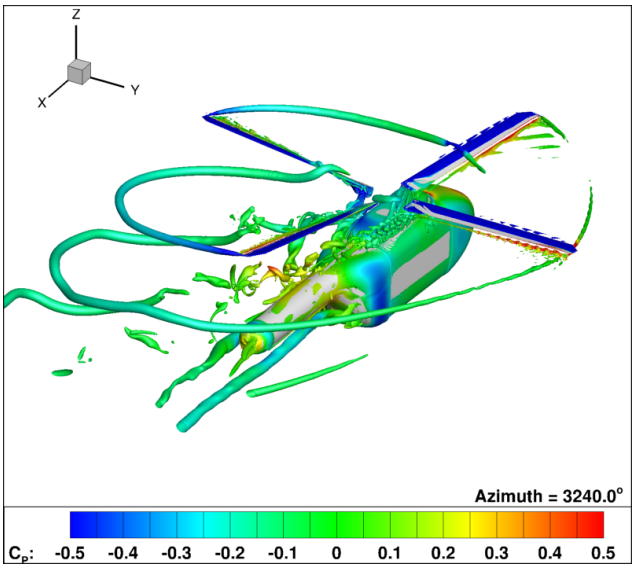

Fig. 45. Baseline (no flow control) case showing an iso-surface contour of the Q-criterion shaded by C_p for forward flight for α =-3°, $U_\infty = 0.2093$,$\mu = 0.35$, and $C_T/\sigma = 0.08$.

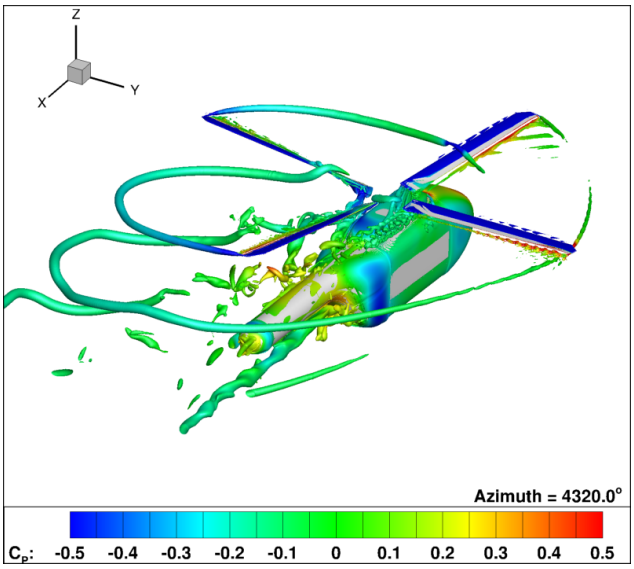

Fig. 46. AFC case showing an iso-surface contour of the Q-criterion shaded by C_p for forward flight for α =-3°, $\mu = 0.35$, $U_\infty = 0.2093$, and $C_T/\sigma = 0.08$.

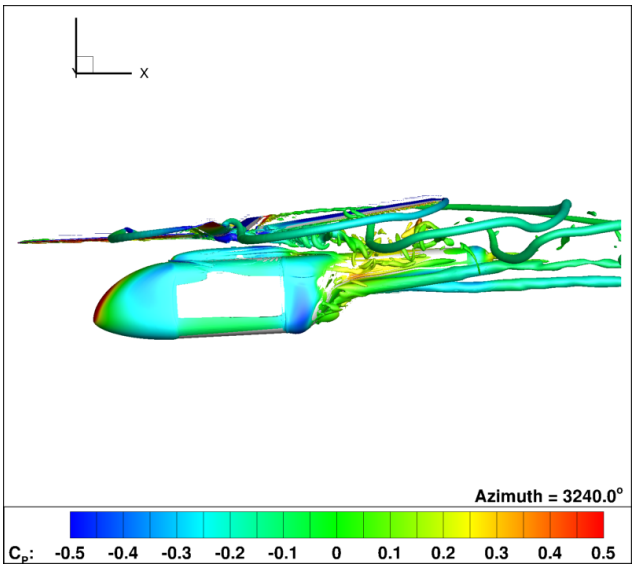

Fig. 47. Baseline (no flow control) case showing a side view of an iso-surface contour of the Q-criterion shaded by Cp for forward flight at α =-3°, $\mu = 0.35$, $U_\infty = 0.2093$, and $C_T/\sigma = 0.08$.

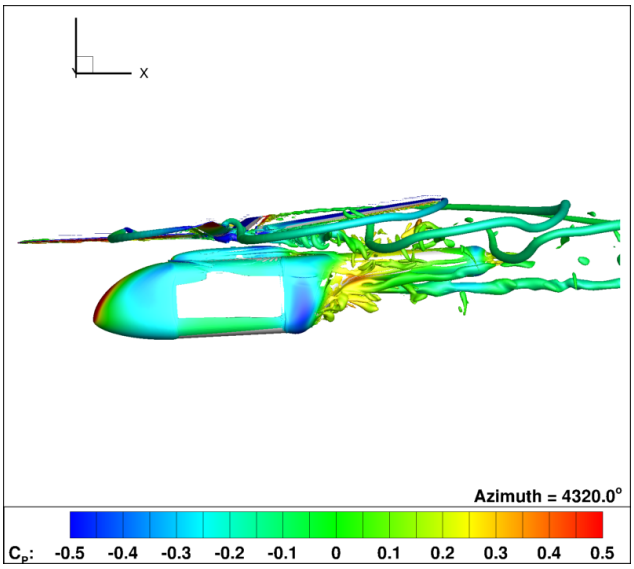

Fig. 48. AFC case showing a side view of an iso-surface contour of the Q-criterion shaded by Cp for forward flight at α =-3°, $\mu = 0.35$, $U_\infty = 0.2093$, and $C_T/\sigma = 0.08$.